**UNIVERSITY OF KWAZULU-NATAL**

# EQUILIBRIUM PROPERTIES OF SOME HIGH-TEMPERATURE SUPERCONDUCTORS

by

**Kalengay Mbela**

Submitted in partial fulfillment of the
requirements for the degree of
Master of Science,
in the
School of Physics,

Durban

December 2007

# PREFACE

This study represents original work by the author and has not been submitted in any form to another University. Where use was made of the work of others it has been duly acknowledged in the text.

*To the Glory of the Lord Jesus Christ.*

**Abstract**

An important fundamental problem in the understanding of the high-$T_c$ superconducting systems is the determination of their equilibrium magnetization behaviour, in particular their constitutive $B^{rev}(H)$ or $M^{rev}(H)$ behavior. Single crystal specimens of these materials are typically small (order of micron/millimeter), and are generally in the form of platelets. Their superconductivity properties are, moreover, highly anisotropic. The magnetization $[M(H_0)]$ curves in these systems also manifest a hysteresis due to vortex pinning, and, at fields below the lower critical field $H_{c1}$, due to a "geometry" effect, which results from a non-uniform internal field distribution in the platelet specimen geometry in a perpendicular applied magnetic field $H_0$.

In the present work a brief review of the field is given and a treatment (due to Doyle and Labusch) of the problem is described in some detail, and is used in the analysis of magnetization data $[M(H_0)]$ on single-crystal platelet specimens of the YBCO and BSCCO high-$T_c$ superconducting systems. The treatment, which is based on a rigorous theoretical analysis of a quasi-static arbitrary distribution of vortices in a specimen of arbitrary shape (Labusch and Doyle ), predicts the quasi-static magnetization behavior $M(H)$ of the specimen, and allows for the inclusion of explicit relations for the equilibrium "constitutive" $B^{rev}(H,T)$, and for the bulk vortex pinning force density $P_v(B)$. An analytical formula for $B^{rev}(H,T)$ in terms of the fundamental characteristic properties $\kappa_{ij}(T)$ (the anisotropic Ginsburg -Landau parameter) and the critical field $H_c(T)$ (or the lower critical field $H_{c1}(T)$) is obtained from an accurate model fit to a numerical solution of the non-linear Ginsburg-Landau equation (Labusch and Doyle ).

For the determination of $\kappa$ and $H_{c1}^c$, (i.e. the G-L parameter and the lower critical field along the crystalline c- axis of platelet specimens) from $M(H_0,T)$ experimental isotherms (where $H_0$ is the magnetic field applied along the c-axis -the thin dimension of the platelet specimens), a computer algorithm, which incorporates the above treatments, was used. In order to obtain a fit between theoretical model results (of the numerical algorithm for equilibrium behavior) and the experimental $M(H_0,T)$ data, experimentally obtained

hysteresis curves were averaged by taking the mean values of $M(H_0)$ for $H_0$ increasing and decreasing over the entire $M(H_0)$ loop. This data was then normalized by $H_{c1}(T)$ for both $M$ and $H_0$, with $H_{c1}(T)$ and $\kappa(T)$ being used as fitting parameters.

# ACKNOWLEDGEMENTS

The author wishes to thank the following people for their respective roles in the compilation of this thesis:

- My Supervisor, Professor T.B. Doyle, of the School of Physics, for his patience, willingness, understanding, expert guidance, and precious input.
- My family for their love, support, words of encouragement, prayer and time.
- The National Research Foundation (NRF) for financial support.
- My co-supervisor Prof P. Sadha and Dr T. Moyo of the School of Physics, for their support, and encouragement.
- All my colleagues and friends for their encouragement and input.

# Contents

# List of Figures

# List of Tables

# Chapter 1

# INTRODUCTION TO FUNDAMENTAL THEORY

## 1.1 Historical Preview

A Dutch physicist, Kamerlingh Onnes [1], having produced liquid Helium, discovered superconductivity in 1911. He observed that the resistivity of mercury disappeared suddenly at a temperature near 4.2K, the boiling point of liquid Helium at normal atmospheric pressure. The phenomenon was better understood only after perfect diamagnetism was detected in a superconductor by Karl W. Meissner and R. Ochsenfeld [2] of Germany in 1933. This effect is now called the Meissner effect and is recognized as one of the most fundamental characteristics of superconductivity.

In 1950, a treatment of superconductivity was devised by Landau and Ginsburg [3]. This theory, which combined Landau's theory of second-order phase transitions with a Schrödinger-like wave equation for the order parameter, had great success in explaining the macroscopic properties of superconductors. Abrikosov [4] later showed that Ginsburg-Landau theory predicts the division of superconductors into the two categories now referred to as Type I and Type II. He solved the G-L equations for $\kappa \geq 1/\sqrt{2}$ and predicted the vortex (or mixed) state that characterizes type II superconductors.

A fully microscopic theory of superconductivity, however, was not realized until 1957, when the American physicists John Bardeen, Leon N. Cooper and John R. Schrieffer published

the now celebrated BCS theory [5], for which the three were awarded the 1972 Nobel Prize in physics. The theory describes superconductivity as a quantum phenomenon, in which pairs of conduction electrons with equal and opposite spin and momentum are coupled to form Bosons, which are known as "Cooper pairs". An extension of the G-L theory, known as the Ginsburg-Landau-Abrikosov-Gorkov (GLAG) [6] theory, has since been considered as a microscopic description.

In 1962 the British physicist Brian D. Josephson [7] considering the quantum nature of superconductivity, proposed, that superconducting pairs can tunnel through a barrier. The effect, known as the Josephson effect, subsequently was confirmed by experiments. Note: Ginsburg, Landau, and Josephson were also awarded Nobel Prizes.

A decisive breakthrough in superconductivity occurred in April 1986, when Bednorz and Müller [8] discovered that an oxygen-deficient copper oxide compound of a Ba-La-Cu-O system was superconducting with a critical temperature of about 30K. This transition temperature is higher than the maximum allowed by the BCS theory. With this work, Bednorz and Müller set the scene for an explosion of research interest in this new class of materials with a different superconducting mechanism. They were subsequently awarded the Nobel Prize for Physics in 1987.

Inspired by the work of Bednorz and Müller, condensed matter physicists and materials scientists around the world began to search for superconducting compounds possessing even higher critical temperatures. Soon after this, Chu et al. [9], achieved a transition temperature of about 90K in ceramics of the system $Y_1Ba_2Cu_3O_{8-x}$, $0 < x < 1$. In 1988, many new ceramic oxide superconducting compounds and classes of compounds were discovered. Notable among these were the Bi-Sr-Cu-O and the Bi-Sr-Ca-Cu-O (BSCCO) compounds, with transition temperatures up to 115K, and the Tl-Ba-Ca-Cu-O (TBCCO) compounds, with transition temperatures up to 125K. There are many other widely known "high-$T_c$ " superconductors and the family is now very large. A more complete list of superconducting materials and their critical temperatures can be found in a review article by Harshaman and Millis [10].

## 1.2 The Meissner – Ochsenfeld Effect

The Meissner effect is the total exclusion of magnetic flux from the interior of a superconductor, i.e. perfect diamagnetism. It was discovered by Walter Meissner and Robert Ochsenfeld [2] in 1933. The Meissner effect is one of the defining features of superconductivity and its discovery served to establish that the onset of superconductivity is a phase transition. Meissner and Ochsenfeld found that when a superconductor is cooled below $T_c$ in a weak applied magnetic field $\boldsymbol{H}_0$ less than some characteristic field $\boldsymbol{H}_c$, the induction $\boldsymbol{B}$ is excluded from the specimen, i.e. $\boldsymbol{B} \rightarrow 0$. This is illustrated in Fig. 1.1. Consider an

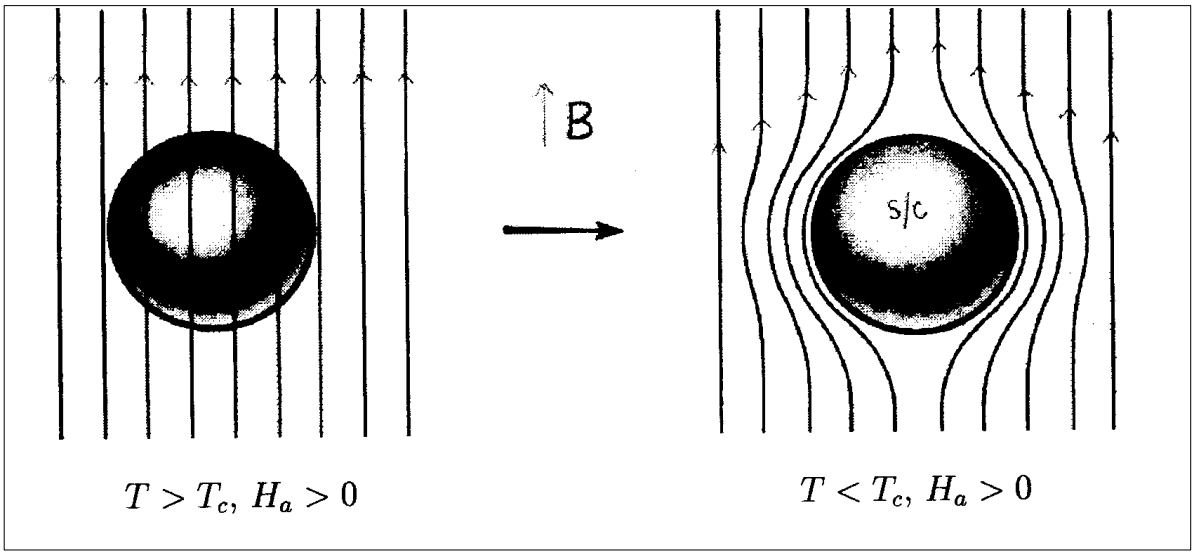


FIG. 1.1. Illustration of the Meissner effect [2].

infinitely long cylindrical specimen, i.e. one with zero demagnetizing coefficient, with the magnetic field, $\boldsymbol{H}_0$ applied parallel to its axis. For $T < T_c$ and $\boldsymbol{H}_0 < \boldsymbol{H}_c$, the induction $\boldsymbol{B}$ inside the specimen is given by $\boldsymbol{B} = 0 = \boldsymbol{H}_0 + 4\pi\boldsymbol{M}$ (emu), where $\boldsymbol{M}$ is the specimen magnetization. For a specimen with non-zero demagnetizing coefficient $D$, we have: $\boldsymbol{B} = 0 = \boldsymbol{H}_0 + 4\pi\boldsymbol{M}(1 - D)$ in the Meissner state [2].

## 1.3 Elementary phenomenological theory

### 1.3.1 Thermodynamics

The superconducting state is a lower energy state than the normal state. In this section we consider the thermodynamic critical field $\boldsymbol{H}_c$, at which the material undergoes a superconducting to normal transition. At this field, the work done in magnetic expulsion is equal to the zero-field energy difference between the normal and superconducting states. When the magnetic field is monotonically increased in the Meissner state, the difference between $G_s$ and $G_n$, the Gibbs free energy of the normal and superconducting states, decreases with the magnetic field. At some point, the internal field reaches $\boldsymbol{H}_c$, and there is a first-order phase transition from the superconducting to the normal state and specified by:

$$G_n(T, \boldsymbol{H}_c) = G_s(T, \boldsymbol{H}_c)\,. \tag{1.1}$$

Thermodynamic consideration yields an expression [11], namely:

$$G_n(T, \boldsymbol{H}_c) - G_s(T, \boldsymbol{H}_c) = \frac{\boldsymbol{H}_c^2}{8\pi}\,. \tag{1.2}$$

The precise form of $\boldsymbol{H}_c\,(T)$ depends on the detailed microscopic theory, but an approximate temperature dependence for $\boldsymbol{H}_c$ is given by [11]:

$$\boldsymbol{H}_c(T) = \boldsymbol{H}_c(0)\left[1 - (T/T_c)^2\right]\,, \tag{1.3}$$

where $\boldsymbol{H}_c(0) = \boldsymbol{H}_c(T = 0)$.

### 1.3.2 The London equations

The Two-Fluid model proposed by Gorter and Casimir [12] in 1934 was successful in explaining some properties of superconductors. In 1935, F. London and H. London [13] used this model to develop expressions for magnetic field penetration and current distribution within a superconducting material. They assumed that the superconducting fraction $n_s$ of the total electron density, $n$, is not scattered by crystalline impurities or phonons and consequently does not contribute to the electrical resistance. The equation of motion for

superconducting electrons of mass $m$, local drift velocity $\boldsymbol{v_s}$ and charge $e$, freely accelerated in an electric field $\boldsymbol{E}$, is given by:

$$m\dot{\boldsymbol{v}}_s = e\boldsymbol{E}\,, \tag{1.4}$$

The superfluid current density

$$\boldsymbol{J_s} = n_s e\boldsymbol{v_s}\,, \tag{1.5}$$

can then be re-written as

$$\dot{\boldsymbol{J}}_{\boldsymbol{s}} = \left(\frac{n_s e^2}{m}\right)\boldsymbol{E}\,. \tag{1.6}$$

Maxwell's equation relating the electric field $\boldsymbol{E}$ to the local microscopic field, $\boldsymbol{h}$ [note: $\boldsymbol{B}$ is the average of $\boldsymbol{h}$], is given by:

$$\boldsymbol{\nabla}\times\boldsymbol{E} = -\frac{1}{c}\frac{\partial\boldsymbol{h}}{\partial t}\,, \tag{1.7}$$

where $\boldsymbol{E} = \rho\boldsymbol{J}$ ( with $\rho$ the resistivity of the material). Substituting Eq. (1.6) into Eq. (1.7), and re-arranging terms, yields:

$$\frac{\partial}{\partial t}\left(\boldsymbol{\nabla}\times\boldsymbol{J} + \frac{n_s e^2}{mc}\boldsymbol{h}\right) = 0\,. \tag{1.8}$$

As the resistivity $\rho \to 0$ (as is the case for a perfect conductor), the left-hand side of Eq. (1.7) approaches zero resulting in the microscopic field $\boldsymbol{h}$, and hence $\boldsymbol{B}$, being constant and not zero. This contradicts the observations of Meissner and Oschenfeld. Incidentally, we see that the Meissner effect is an inherent feature of the superconducting state and not a consequence of zero resistivity. To avoid this contradiction, F. London and H. London integrated Eq. (1.8) and obtained a result known as the first London equation:

$$\boldsymbol{\nabla}\times\boldsymbol{J} + \left(\frac{n_s e^2}{mc}\right)\boldsymbol{h} = 0. \tag{1.9}$$

This equation does account for flux expulsion and also provides a definition for the magnetic penetration depth, $\lambda$. Substituting the Maxwell equation $\boldsymbol{\nabla}\times\boldsymbol{h} = (4\pi/c)\,\boldsymbol{J}$, into Eq. (1.9), and using the vector identity $\boldsymbol{\nabla}\times\boldsymbol{\nabla}\times\boldsymbol{A} = \boldsymbol{\nabla}(\boldsymbol{\nabla}\cdot\boldsymbol{A}) - \boldsymbol{\nabla}^2\boldsymbol{A}$, together with $\boldsymbol{\nabla}\cdot\boldsymbol{h} = 0$, yields:

$$\boldsymbol{\nabla}^2\boldsymbol{h} - \left(\frac{4\pi n_s e^2}{mc^2}\right)\boldsymbol{h} = 0\,, \tag{1.10}$$

which can also be written as

$$\boldsymbol{\nabla}^2\boldsymbol{h} - \frac{1}{\lambda^2}\boldsymbol{h} = 0\,. \tag{1.11}$$

Here

$$\lambda = (\frac{mc^2}{4\pi n_s e^2})^{1/2}\,, \tag{1.12}$$

has the units of length and is known as the **London penetration depth** For an infinite slab of superconductor filling the half-space $x > 0$, the one-dimensional form of Eq. (1.11) is given by

$$\frac{d^2}{dx^2}\boldsymbol{h}(x) - \frac{1}{\lambda^2}\boldsymbol{h}(x) = 0\,, \tag{1.13}$$

and the field inside the superconductor is given by

$$\boldsymbol{h}(x) = \boldsymbol{H}_o \exp(-x/\lambda)\,, \tag{1.14}$$

where $\boldsymbol{H}_o$ is the field applied parallel to the superconductor surface. From Eq. (1.14) it is clear that deep within the SC (i.e. as $x \to \infty$) the microscopic field $\boldsymbol{h}(x) \to 0$ and we have the Meissner state. The penetration depth $\lambda$ is also the characteristic depth within which the screening currents flow in order to exclude the applied magnetic field. The superconducting current $\boldsymbol{J}$, is given in terms of the vector potential $\boldsymbol{A}$, by:

$$\boldsymbol{J}(r) = -\frac{n_s e^2}{mc}\boldsymbol{A}(r) = -\frac{c}{4\pi}\frac{1}{\lambda^2}\boldsymbol{A}(r)\,. \tag{1.15}$$

This equation is another expression of the London equation. Whilst the London equation is successful in describing the Meissner effect and providing a definition for the penetration depth, the equation is deficient in that: (i) it is a local theory and is not strictly valid for a type-I superconductor in which the electrodynamics are non-local and (ii) it offers no explicit temperature dependence for the superconducting electron density, $n_s$ [13].

### 1.3.3 The Ginsburg-Landau theory

The GL theory introduces a macroscopic wave function, $\psi(\boldsymbol{r})$ as an order parameter to describe the superconducting electrons and expressed by:

$$\psi\left(\boldsymbol{r}\right) = \left|\psi\right| e^{i\varphi(\boldsymbol{r})}\,, \tag{1.16}$$

where $\varphi\left(\boldsymbol{r}\right)$ and $\psi\left(\boldsymbol{r}\right)\psi^*\left(\boldsymbol{r}\right) = n_s\left(\boldsymbol{r}\right)$ are the phase and the superconducting electron density, respectively, at a point $\boldsymbol{r}$. The superconductor free energy density [14] is then

expressed as an expansion in even powers of $|\psi|^2$, plus kinetic and field energy terms, thus:

$$G_s(\boldsymbol{r},T) = G_n(\boldsymbol{r},T) + \alpha\,|\psi|^2 + \frac{\beta}{2}\,|\psi|^4 + \frac{1}{2m^*}\left|\left(\frac{\hbar}{i}\boldsymbol{\nabla} - \frac{e^*}{c}\boldsymbol{A}\right)\psi\right|^2 + \frac{h^2}{8\pi}\,, \tag{1.17}$$

where $\alpha$ and $\beta$ are two phenomenological material dependent parameters , $\boldsymbol{A}$ is the vector potential of the magnetic field. The first term on the right-hand-side of Eq. (1.17) describes the normal state free energy $G_n$. The second and the third terms contain the power law expansion of the condensation energy in terms of $|\psi|^2$. The fourth term represents the kinetic energy of the super electrons and the last term is the field energy. Minimization of Eq. (1.17) with respect to the order parameter $\psi$, and the vector potential $\boldsymbol{A}$ , yields a pair of coupled equations given by:

$$\alpha\psi + \beta\,|\psi|^2\,\psi + \frac{1}{2m^*}\left|\frac{\hbar}{i}\boldsymbol{\nabla} - \frac{e^*}{c}\boldsymbol{A}\right|^2\psi = 0\,, \tag{1.18}$$

and

$$\boldsymbol{J} = \frac{c}{4\pi}\boldsymbol{\nabla}\times\boldsymbol{h} = \frac{e^*\hbar}{2m^*i}\left(\psi^*\boldsymbol{\nabla}\psi - \psi\boldsymbol{\nabla}\psi^*\right) - \frac{e^*}{m^*c}\psi^*\psi\boldsymbol{A}\,. \tag{1.19}$$

The solution of these two GL equations provides a good understanding of superconductivity in terms of just a few parameters [14].

**Thermodynamic critical field**

The phenomenological parameter, $\alpha$, introduced in Eq. (1.17) is approximated by a first-order Taylor expansion such that $\alpha = \alpha_0(T - T_c)$. This means that $\alpha$ is positive in the normal state and negative in the superconducting state. $\beta$ is a positive, temperature-independent constant. Minimization of the free energy results in the usual London theory as the first, second and third terms of Eq. (1.17) are all constants in this theory. Similarly, if there is no magnetic field and the order parameter has no phase $\varphi$ then the fourth and fifth terms of Eq. (1.17) are zero and the free energy difference between the normal and superconducting state becomes:

$$G(\psi,T) \approx \alpha(T)\,|\psi|^2 + \frac{1}{2}\beta\,|\psi|^4 \tag{1.20}$$

Minimizing with respect to $|\psi|^2$ gives:

$$\frac{dG}{d\,|\psi|^2} = \alpha(T) + \beta\,|\psi|^2 = 0\,. \tag{1.21}$$

Hence

$$|\psi|^2 = -\frac{\alpha(T)}{\beta} \approx n_s \,. \tag{1.22}$$

Substituting back into Eq. (1.17), in the absence of fields and currents, results in the following expression:

$$G_s - G_n = -\frac{\alpha^2(T)}{2\beta} \,. \tag{1.23}$$

A comparison of Eqs. (1.2) and (1.23) shows that $H_c^2/8\pi = \alpha^2(T)/2\beta$.

### Magnetic penetration depth

Variations of the order parameter $\psi$ can be neglected in a small magnetic field. The second G-L Eq. (1.19) can then be written as:

$$\boldsymbol{J} = -\frac{e^* |\psi|^2}{m^*} \boldsymbol{A} \,. \tag{1.24}$$

Re-defining $\lambda$ in the form :

$$\frac{1}{\lambda^2} = \frac{4\pi e^{*2} |\psi|^2}{m^* c^2} \,, \tag{1.25}$$

again yields the London equations. The temperature dependence of the penetration depth is given by [14]:

$$\lambda^2(T) \propto \frac{1}{T_c - T} \,. \tag{1.26}$$

### Coherence length

According to the G-L theory, a coherence length, $\xi_{GL}$, can be defined as a characteristic distance over which spatial changes in the superconducting order parameter $\psi$ occur. Eq. (1.18) for the one-dimensional form, in the absence of an external magnetic field, can be written as:

$$-\frac{\hbar^2}{2m^*} \frac{d^2\psi}{dx^2} + \alpha\psi + \beta |\psi|^2 \psi = 0 \,. \tag{1.27}$$

Solving this equation for certain conditions which should be stated, e.g $\psi \to 0$ as $x \to 0$, $\psi \to \psi_0$ as $x \to \infty$, yields:

$$\psi = \psi_0 \left[ 1 - \exp\left( -\frac{\sqrt{2}x}{\xi_{GL}(T)} \right) \right] \,. \tag{1.28}$$

where the Ginsburg-Landau coherence length, $\xi_{GL}$ is given by:

$$\xi_{GL}(T) = \sqrt{\frac{\hbar^2}{2m^* \left|\alpha(T)\right|}} \quad . \tag{1.29}$$

and has the dimensions of length. The temperature dependence of the coherence length is given by [14]: $\xi(T) \propto (T_c - T)^{-1/2}$ i.e. the same as for $\lambda_{GL}$ and diverges near $T_c$.

### The Ginsburg-Landau parameter

In the original form of the G-L theory, the two lengths $\lambda$ and $\xi$ have the same dependence on $\alpha$, and hence on $T$: i.e. they both diverge as $(T_c - T)^{-1/2}$ as $T_c$ is approached from below. Their ratio $\kappa = \lambda/\xi$, is an important parameter of the theory known as the Ginsburg-Landau parameter, and inter alia, it determines whether the material is a Type I or a Type II superconductor. This parameter may be written as:

$$\kappa = \sqrt{\frac{m^2\beta}{2\pi\hbar^2 e^2}}\,. \tag{1.30}$$

From Eq. (1.30), $\kappa$ is a function of $\beta$ only and is, therefore, approximately independent of $T$ for $T$ near $T_c$. Also, for $\kappa \leq 1/\sqrt{2}$, we have a Type I superconductor and for $\kappa \geq 1/\sqrt{2}$, a Type II superconductor.

### Surface energy

Consider a sample where half the space is superconducting and the other half is normal. The surface energy, $\sigma_s$, of a superconducting-normal boundary is expressed in terms of the difference between the Gibbs free energies by:

$$\sigma_{ns} = \int_{-\infty}^{\infty} (G(x) - G_n(x))dx\,, \tag{1.31}$$

where $G(x)$ is the Gibbs free energy of the system, equal to $G_n$ for $x < 0$ and to $G_s$ for $x \gg 1$. According to the GL theory, the free energy difference per unit area at a superconducting-normal boundary is given by:

$$\sigma_{ns} = \frac{\boldsymbol{H}_c^2}{8\pi} \int_{-\infty}^{\infty} \left[ \left(1 - \frac{\boldsymbol{h}}{\boldsymbol{H_0}}\right) - \left(\frac{\psi}{\psi_0}\right)^4 \right] dx\,. \tag{1.32}$$

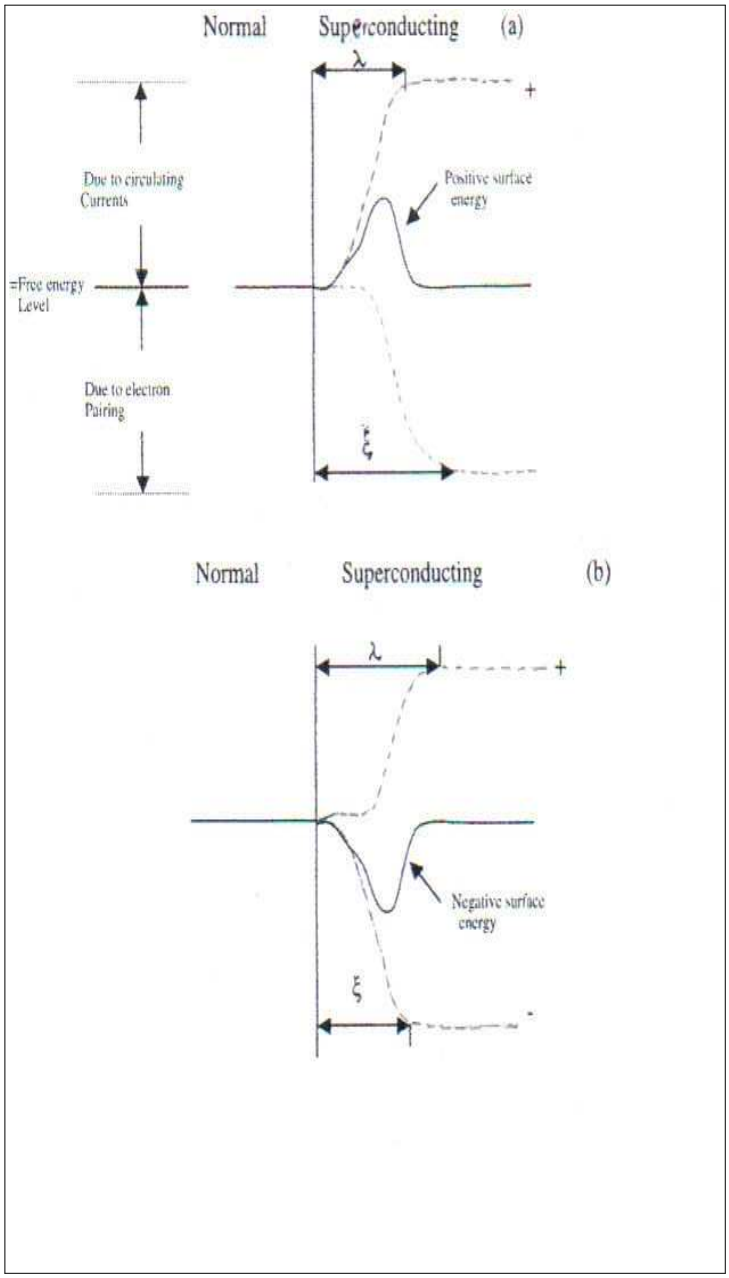


FIG. 1.2. The surface energy at the boundary between normal and superconducting regions, for (a) Type I and (b) Type II materials.

It can be seen from this expression that the sign of $\sigma_{ns}$ is determined by the balance between the positive magnetic expulsion and the negative condensation energies. This is illustrated schematically in Fig. 1.2.

## 1.4 Type I and type II superconductors

1) Type I ($\kappa < 1/\sqrt{2}$)

Type I materials (with zero demagnetizing coefficient), exhibit perfect diamagnetism for the applied field in the range of $0 \leq \boldsymbol{H}_0 \leq \boldsymbol{H}_c$, and enter the normal state for $\boldsymbol{H}_0 > \boldsymbol{H}_c$, as illustrated in Fig. 1.3(a). Ginsburg and Landau solved the G-L Eqs. [(1.18) and (1.19)] for the case $\kappa < 1/\sqrt{2}$, where the net superconducting/normal interface energy, given approximately by:

$$\triangle E = \frac{\boldsymbol{H}_c^2}{8\pi}(\xi - \lambda)\,, \tag{1.33}$$

is positive when the magnetic penetration depth $\lambda$ is smaller than the coherence length $\xi$ [11].

2) Type II ($\kappa > 1/\sqrt{2}$)

In the case of type II superconductors, the perfect diamagnetic (Meissner) response exists below the lower critical field, $\boldsymbol{H}_{c1} < \boldsymbol{H}_c$, given by:

$$\boldsymbol{H}_{c1} = \frac{4\pi\epsilon}{\Phi_0} \simeq \frac{\Phi_0}{4\pi\lambda^2}\ln\kappa\,, \tag{1.34}$$

When the applied field is above $\boldsymbol{H}_{c1}$, as illustrated in Fig. 1.3(b), the flux starts to penetrate the material in the form of quantized flux tubes or vortex. Each vortex contains exactly one magnetic flux quantum of magnitude: $\Phi_0 = \dfrac{hc}{2e} = 2.07{\times}10^{-7}$ gauss cm$^2$, where $h$ is Planck's constant and $e$ is the charge on the electron. As the external field is gradually increased, the density of flux lines increases. Eventually their cores, in which the superconducting order parameter is equal zero, will begin to overlap and the whole medium becomes normal. This intermediate field regime $\boldsymbol{H}_{c1} < \boldsymbol{H}_0 < \boldsymbol{H}_{c2}$ is often referred to as the mixed state or vortex state. The magnetic field strength up to which the mixed state can persist is called the upper critical field $\boldsymbol{H}_{c2}$, and is given by [11]:

$$\boldsymbol{H}_{c2} = \sqrt{2}\kappa\boldsymbol{H}_c(T) = \frac{\Phi_0}{2\pi\xi^2(T)} \tag{1.35}$$

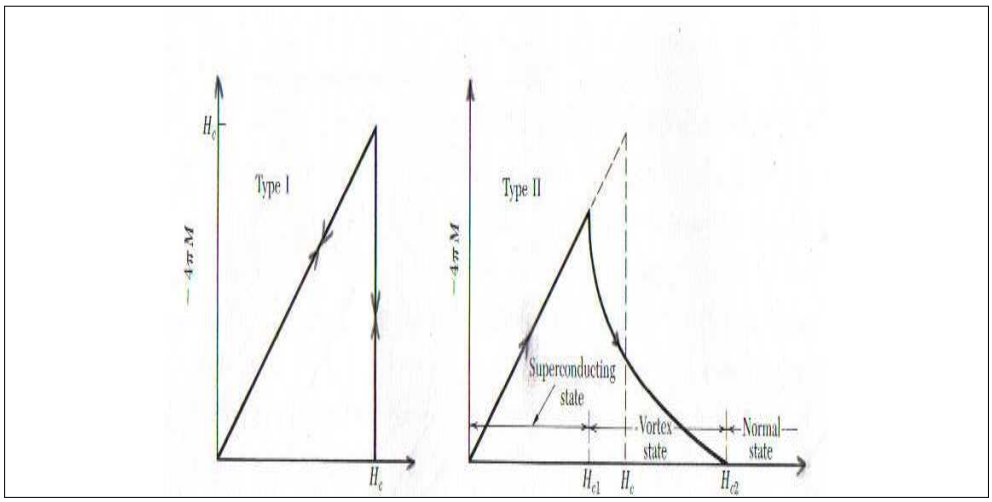


FIG. 1.3. 'Ideal' (reversible) magnetization curves (a) for Type I and (b) for Type II superconductors, with small demagnetizing coefficient [2].

## 1.5 The BCS theory

The BCS theory is a microscopic theory of superconductivity, published in 1957 by Bardeen, Cooper and Schrieffer. It is based on the idea that near the Fermi surface, electrons experience a mutual attraction by the exchange of a virtual phonon and form pairs. The coupled electron pairs, known as "Cooper pairs", have equal and opposite momenta and spins. Cooper pairs are, therefore, bosons and obey, Bose-Einstein statistics. Some of the BCS parameters are briefly introduced below. Bardeen, Cooper and Schrieffer were also awarded a Nobel Prize [5].

### 1.5.1 BCS superconducting Gap Parameter

The BCS theory introduces a temperature-dependent gap parameter, $\Delta(T)$, given by:

$$\Delta(T) = 1.74\,\Delta(0)\,(1 - T/T_c)^{1/2}\ , \tag{1.36}$$

for $T$ near $T_c$. The energy gap at $T = 0$ K is related to $T_c$ by :

$$\Delta(0) = \frac{\beta_c\,\kappa_B\,T_c}{2}\,, \tag{1.37}$$

where $\kappa_B$ is Boltzman's constant, $\beta_c$ is the proportional energy gap constant. For so-called weak-coupled superconductors, experimental values for $\beta_c$ vary from 3.0 to 4.5 with most

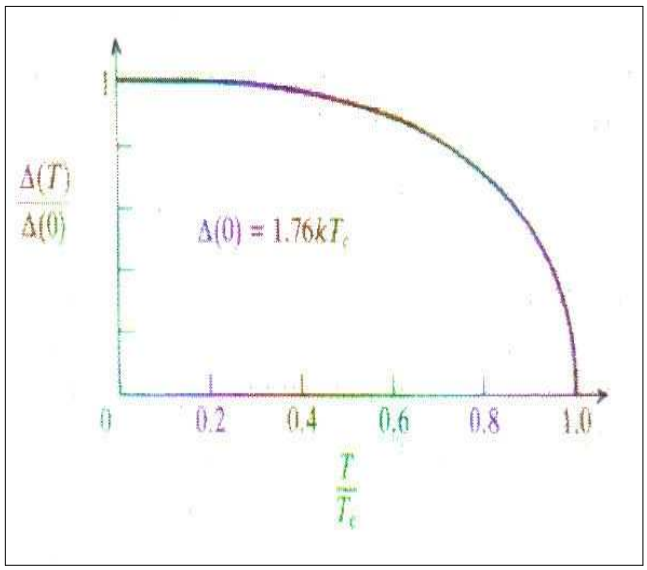


FIG. 1.4. Temperature dependence of the BCS reduced gap parameter, $\Delta(T)/\Delta(0)$ [11].

around the theoretical BCS value of $\beta_c = 3.5$. Fig. 1.4 shows the temperature dependence for the reduced energy gap parameter $\Delta(T)/\Delta(0)$. This temperature dependence is accurately followed in the weak-coupling limit, but remains a relatively good approximation in general.

### 1.5.2 BCS Critical Temperature

According to the BCS theory, the critical temperature $T_c$ is given by:

$$T_c = \frac{1.13\,\hbar\,\omega_D}{k_B} \exp\left(-1/\lambda_{ep}\right) , \tag{1.38}$$

where $\omega_D$ is the Debye frequency and $\lambda_{ep}$, is a dimensionless electron-phonon coupling parameter, which is approximately 0.3 for conventional superconductors. With $\lambda_{ep} = 0.3$, and typical values for $\omega_D$ equal to $10^{12}$ Hz to $10^{13}$ Hz, the BCS theory predicts a maximum $T_c$ of around 25K. This vibration range is equivalent to the Debye temperatures, $\Theta_D = 100\text{K} - 500\,\text{K}$ where $\hbar\omega_D = k_B\Theta_D$.

### 1.5.3 BCS Coherence Length

The BCS theory also introduces a temperature-independent coherence length, $\xi_0$, given by:

$$\xi_0 = 0.18\,\frac{\hbar\, v_F}{k_B T_c}\,, \tag{1.39}$$

where $v_F$ is the Fermi velocity. Taking $v_F = 10^6\,\mathrm{ms}^{-1}$ and $T_c \approx 10\,\mathrm{K}$, yields $\xi_0 \sim 1800\,\text{Å}$. The relation between the temperature-dependent G-L coherence length, $\xi(T)$ and the temperature-independent BCS coherence length, $\xi_0$, depends upon the mean-free path, $\ell_e$, of the electrons. Two limits for $T$ near $T_c$ are considered, namely:

(i) the "clean-limit" ($\ell_e \gg \xi_0$), which yields

$$\xi(T) = 0.74\,\xi_0 \left(\frac{T_c}{T_c - T}\right)^{1/2}\,, \tag{1.40}$$

and

(ii) the "dirty-limit" ($l_e \ll \xi_0$), which yields

$$\xi(T) = 0.85\,\sqrt{\xi_0\,\ell_e}\left(\frac{T_c}{T_c - T}\right)^{1/2}\,. \tag{1.41}$$

### 1.5.4 BCS Penetration Depth

The BCS theory for the penetration depth $\lambda(t)$ on reduced temperature $t = T/T_c$ gives [11]:

$$\lambda(t) = \lambda(0)\left[\frac{\Delta(t)}{\Delta(0)}\tanh\left(\frac{\beta_c}{4t}\frac{\Delta(t)}{\Delta(0)}\right)\right]^n\,, \tag{1.42}$$

where $n = -1/3$ for the "clean-limit" and $n = -1/2$ for the "dirty-limit".

## 1.6 Applications of superconductors

Soon after Kamerlingh Onnes discovered superconductivity, scientists worked hard in order to find practical applications for this new phenomenon. However, it has only found technological applications since about the middle of the $20^{\text{th}}$ century. Since then the low temperature-metallic superconductors, with transition temperatures below about 24K have found many applications. These applications can be categorized in two different groups. The first, related to high- current applications, includes: large electromagnets, urban power reticulation, surge arrestors, energy storage, magnetic bearings, and (now very important) ships motors. The low-current applications include: a large variety of thin-film passive microwave devices, and active devices based on the Josephson junction. With the discovery of high-temperature superconductors, applications currently being explored include: magnetic shielding devices, medical imaging system, infrared sensors, analog signal processing devices. As the understanding of the properties of high-$T_c$ superconducting material increases, these applications will become more widespread.

## 1.7 Aim of this project

The aims are two fold:

(i) to obtain equilibrium $B^{rev}(H)$ behavior and hence parameters $H_c$, $H_{c1}$, $H_{c2}$, $\kappa$ etc, which are of fundamental importance and interest, and

(ii) to resolve the vortex pinning mechanisms.

## 1.8 Our approach

Our approach to the determination of the constitutive $B^{rev}(H)$ behavior uses a theoretical model and an algorithm for its solution that require a analytical formula for $B^{rev}(H)$. This formula, whether, heuristic (as used in earlier work by Doyle and Labusch), or derived from analytical fits to rigorous numerical solutions of the G-L equations (see later) will generally and explicitly include a sufficient number of the above parameters, which will then be treated as fitting parameters when fitting the theoretical prediction to the experimental $M - H$ curves. In the present work the treatment is applied to $M(H_0)$ data for single crystal platelet specimens of the YBCO and BSCCO high-$T_c$ superconducting systems. The investigation is carried out using a computer algorithm which incorporates the above theoretical considerations for a type II superconductor with platelet shape and arbitrary vortex distribution [15]. However, since the experimental $M(H_0)$ curves are hysteretic it is necessary to approximate the equilibrium behavior by taking the mean of the $M(H_0 \uparrow)$ and $M(H_0 \downarrow)$ curves. The experimental $M - H_0$ behavior is then normalized (both $M$ and $H_0$) by a free fitting parameter for the fitting to the theory, in which all magnetic properties are normalized to $H_{c1}$, so that this fitting parameter is then automatically $H_{c1}$ for the bulk of the material. The other obvious fitting parameter is $\kappa$. This provides us with a method for the determination of the superconducting parameters, $\kappa$ and $H_{c1}$.

# Chapter 2

# LITERATURE SURVEY

## 2.1 Introduction

The occurrence of the mixed state was predicted by Abrikosov [4] in 1957. From analytical solutions of Ginsburg-Landau equations [3] in the regime where the Ginsburg-Landau parameter $\kappa$ is greater than $1/\sqrt{2}$, he obtained results for both the upper and lower critical fields, $\boldsymbol{H}_{c2}$ and $\boldsymbol{H}_{c1}$, respectively. Abrikosov not only theoretically described the magnetic behavior of Type II superconductors, but also predicted the vortex " Shubnikov" phase (or the mixed-state phase). Since then the equilibrium mixed-state structure has been the subject of much theoretical and experimental study. The determination of the reversible magnetization, $\boldsymbol{M}^{rev}(\boldsymbol{H})$, or $\boldsymbol{B}^{rev}(\boldsymbol{H})$, is an important aspect of the physics of type II superconducting systems. In this chapter we review some fundamental aspects of vortex structure, the vortex lattice (mixed-state phase), vortex pinning, the geometry effect, and the surface barrier effect (i.e. the barrier to vortex penetration at a superconducting/normal interface).

## 2.2 GL Theory

### 2.2.1 A single isolated Abrikosov vortex

The basic unit of the mixed state is the flux vortex containing one quantum of magnetic flux. Fig. 2.1 illustrates what is meant by a vortex line in the mixed state.

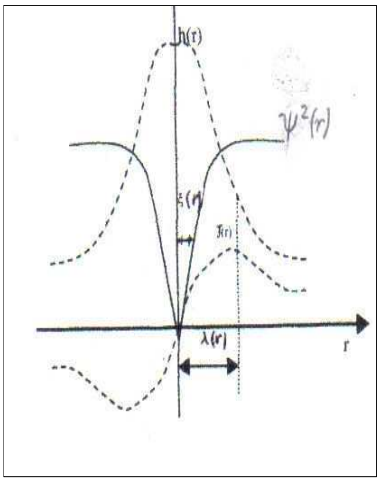


FIG. 2.1. Distributions of $|\psi|^2$, $\boldsymbol{J}(r)$, and $\boldsymbol{h}(r)$ near a single Abrikosov vortex.

The magnetic field $\boldsymbol{h}$ and the order parameter $|\psi|^2$ are represented as a function of distance from the vortex axis if we consider the vortex line as having a cylindrical symmetry. The magnetic field is maximum near the centre of the line. This field is screened by the circulating supercurrents $\boldsymbol{J}(r)$. The magnetic field decays exponentially with distance from the center over the characteristic length $\lambda$ (the penetration depth). At the axis of the vortex the superconducting order parameter characteristic is equal to zero. It increases from the vortex core to its asymptotic limit over a characteristic distance given by the Ginsburg-Landau coherence length $\xi$. The magnetic field and circulating currents decrease rapidly to zero beyond the London penetration depth $\lambda$ [16].

### 2.2.2 Vortices interactions

In an ideal, defect free material, the vortices, because of their mutual repulsive interaction, form a regular 2D lattice, which is normally triangular and has elastic properties.

This equilibrium configuration may be disturbed by crystalline imperfections and inhomogeneities, such as point defects, dislocations, grain boundaries and precipitates, which exert a pinning force on the flux lines. In the presence of a transport current density $\boldsymbol{J}$, there is a local Lorentz force $\boldsymbol{J} \times \boldsymbol{B}$ acting locally on the vortex lattice. If the local Lorentz forces exceed the local pinning force density, the vortices move and generate an e.m.f, which leads to dissipation. In equilibrium the transport current is at its critical value $\boldsymbol{J}_c$ such that $\boldsymbol{J}_c \times \boldsymbol{B} = \boldsymbol{P}_v$, where $\boldsymbol{P}_v$ is the bulk pinning force density. In the critical state, thermal activation of the vortex lattice out of its pinning centres leads to "flux creep" with a non zero, but small dissipation. It is clear that only sufficient strong vortex pinning forces will allow zero-resistance operation in the mixed phase, with a steady critical current.

## 2.3 Geometry effect problem

The geometry effect is among the properties of particular interest in the high-$T_c$ ceramic superconducting systems where single crystals specimens are usually in the form of thin platelets. This effect was first investigated and explained in niobium disc specimens by Doyle [17]. When the applied magnetic field $\boldsymbol{H}_0$ is normal to the plane of the specimen, there is a delay for first penetration of flux (vortices) into the bulk of the specimen, above the predicted value for the inscribed ellipsoid, [i.e., $\boldsymbol{H}_{c1}(1-D)$], where $D$ is the appropriate demagnetizing coefficient (i.e. that for the inscribed ellipsoid). After initial penetration, the vortices tend to accumulate in a pool near the center of the specimen. This pool grows in diameter until at $\boldsymbol{H}_0 \simeq \boldsymbol{H}_{c1}$ the pool fills the specimen. Then in decreasing field, the pool must expand to fill the specimen in order for the flux to be able to exit the specimen. The magnetization behavior therefore displays a hysteresis. The first rigorous and general theoretical treatment is by Labusch and Doyle [18] and Doyle and Labusch [19]. In the latter treatment the Gibbs free energy $\Delta G$ required to create a vortex in a specimen of platelet shape and containing an arbitrary distribution of other vortices, is rigorously derived to be given by:

$$\Delta G = \Phi_0 \int (\boldsymbol{H}^{rev} - \boldsymbol{H}^{e})\, d\boldsymbol{l}\,, \tag{2.1}$$

where the line integral is taken over the length of the vortex. Here $\Phi_0 = hc/2e$ is the flux quantum and, $\boldsymbol{H}^{rev}(\boldsymbol{B}) = (\boldsymbol{B}/B)H^{rev}(B)$ is the reversible field. The local field, $\boldsymbol{H}^e$ is calculated from the following equations:

$$\sigma(\boldsymbol{r}_s) = H^e_\perp - B_\perp/4\pi\,, \tag{2.2}$$

and

$$\boldsymbol{H}^e(\boldsymbol{r}) = \boldsymbol{H}_0 + \frac{1}{4\pi}\iint \frac{\sigma(\boldsymbol{r}_s)(\boldsymbol{r}-\boldsymbol{r}_s)d^2\boldsymbol{r}_s}{|\boldsymbol{r}-\boldsymbol{r}_s|^3}\,, \tag{2.3}$$

where $\sigma(\boldsymbol{r}_s)$ is a surface magnetic charge density, $H^e_\perp$ and $B_\perp$ are the normal components of $\boldsymbol{H}^e$ and $\boldsymbol{B}$ at the specimen surface respectively, and $\boldsymbol{H}_0$ is a uniform applied field. The integral in Eq. (2.3) is taken over the specimen surface, where the tangential component $H^{rev}_\parallel$, is equal to $H^e_\parallel$. The net force acting on a unit length of vortex in an arbitrary distribution of other vortices is

$$\boldsymbol{f} = \Phi_0[(\boldsymbol{\nabla}\times\boldsymbol{H}^{rev})\times\boldsymbol{B}]\times\boldsymbol{B}/B^2 + \boldsymbol{f}_p\,, \tag{2.4}$$

where $\boldsymbol{f}_p$ is a pinning force due to material imperfections. In the critical state, $\boldsymbol{f} = 0$ and $|\boldsymbol{f}_p|$ is the maximum pinning force. In solving the above equations, Labusch and Doyle give a complete description of the quasi-static magnetic behavior of a type II superconductor of platelet shape. In a following paper Doyle and Labusch [19] adapt this treatment to the special case of a disc-shaped type II superconducting specimen in perpendicular applied field. In these earlier papers they use a simple phenomenological expression for the inverse $\boldsymbol{B}^{rev}(\boldsymbol{H})$ of the form:

$$H^{rev}[B] = [B + \gamma(B_{c2} - B) + B_\gamma(1-\gamma)\times\exp(-\alpha B/B_\gamma)]/4\pi\,, \tag{2.5}$$

where $\gamma = [1.16(2\kappa^2-1)]^{-1}$, $B_\gamma = (1-\gamma B_{c2})/(1-\gamma)$ and $B_{c2} = \beta\kappa^2\ln\kappa$. The parameters $\alpha\,,\beta$ and $\kappa$ were obtained empirically by fitting to the $M - H_0$ data for a disc-shaped specimen. In later work where the emphasis moved from an investigation of the geometry effect and vortex pinning behavior to a more detailed study of the equilibrium behavior, a more rigorous expression based on the solution of the GL equation has been formulated and is discussed below.

## 2.4 An analytical formula for $B^{rev}(H)$ (and hence $H^{rev}(B)$) from a solution of the Ginsburg-Landau equations for $\kappa \geq 1/\sqrt{2}$ in uniaxial anisotropic materials.

For the purposes of the present investigation, which uses the Labusch/Doyle treatment and includes the geometry effect, an accurate analytical formulae for the constitutive relation $H^{rev}(B)$ is required. Such an expression has been published by Hao *et al* [16] for the isotropic case and is summarized below.

The equilibrium magnetic field is given by:

$$H^{rev}(B) = \frac{1}{2}\frac{\partial F(B,T)}{\partial B}\,, \tag{2.6}$$

where $F$ is the free energy density of the vortex lattice and is given by:

$$F = F_{em} + F_{ck}\,. \tag{2.7}$$

The first term of Eq. (2.7) is associated with the magnetic field and supercurrents in the vortex lattice, while the second term is associated with the loss of condensation energy in the vortex cores. The final expression for $H^{rev}(B)$ can be written as:

$$H^{rev} = H_{em} + H_{ck}\,, \tag{2.8}$$

where

$$H_{em} = B + \frac{f_\infty}{2\kappa\xi K_1\left(f_\infty\xi\right)}\left[K_0\left(\xi\sqrt{f_\infty^2+2B\kappa}\right) - \frac{\beta\kappa\xi K_1\left(\xi\sqrt{f^2+2B\kappa}\right)}{\left(\xi\sqrt{f_\infty^2+2B\kappa}\right)}\right]\,, \tag{2.9}$$

with $K_0$ and $K_1$ two modied Bessel functions of zero and first order (Hankel functions), and

$$H_{ck} = \frac{\kappa f_\infty^2\xi^2}{2}\left[\frac{1-f_\infty^2}{2}\ln\left(\frac{2}{B\kappa\xi^2}+1\right) - \frac{1-f_\infty^2}{2+B\kappa\xi^2} + \frac{f_\infty^2}{\left(2+B\kappa\xi^2\right)2}\right] + \frac{f_\infty^2\left(2+3B\kappa\xi^2\right)}{2\kappa\left(2+B\kappa\xi^2\right)^3}\,. \tag{2.10}$$

In the equations above, $\xi$ is the coherence length and $f$ is the superconducting order parameter approximated by:

$$f = f_\infty\frac{r}{\sqrt{\left(r^2+\xi^2\right)}}\,, \tag{2.11}$$

where $r$ is the distance from the vortex core and $f_\infty$ is a fit parameter, which is unity at $B = 0$ and decreases to zero at $B = B_{c2}$. The above analysis gives a fairly accurate analytical expression for $H^{rev}(B)$ in high $\kappa$ material. However at low $B$ and low $\kappa$ because of a poor approximation of a trial function for the order parameter $f$, Eq. (2.11), the expression for $H^{rev}(B)$ is inaccurate. The treatment is consequently not good enough for our purposes and, moreover, gives rise to instabilities and to unreasonable values in calculations of the driving force on vortices in the presence of a flux gradient near the lower critical field $H_{c1}$. Labusch and Doyle [15] have modified this treatment and extended it to anisotropic materials by deriving an exact analytical formula for all $B$ and $\kappa \geq 1/\sqrt{2}$. In the calculations of $H^{eq}(B, \kappa)$, they derive $F_{ck}$ and $F_{em}$, by considering the unit vortex cell as having a circular cross section. They considered the Ginsburg-Landau equations in a reduced form using cylindrical coordinates as:

$$\frac{dh}{dr} = f^2 \left( a - \frac{1}{\kappa\, r} \right) , \tag{2.12}$$

and

$$\frac{1}{r}\frac{d}{dr}\left( r\frac{df}{dr} \right) = -\kappa^2 f \left( 1 - f^2 \right) + \left( a - \frac{1}{\kappa r} \right)^2 . \tag{2.13}$$

Here $f$ is the local order parameter approximated by the exponential relation $(1 - f) \propto \exp(-\kappa r/2)$, $\boldsymbol{h}$ is the local magnetic field, and $\boldsymbol{a}$, the vector potential of $\boldsymbol{h}$, is given by:

$$a(r) = \frac{1}{r} \int_0^r h(r') r'\, dr' . \tag{2.14}$$

The boundary conditions are $(dh/dr)_{r=R} = 0$, and $f(r = 0) = 0$. According to Eq. (2.12), $(a(R) - 1/\kappa R) = 0$, and therefore Eq. (2.14) yields:

$$2\pi \int_0^R h(r)\, r\, dr = \frac{2\,\pi}{\kappa} . \tag{2.15}$$

which is the condition that each cell contains one quantum of flux. After solving Eqs. [(2.12) and (2.13)] by an iterative process for the uniaxial anisotropic case, they obtained the following results:

$$H_z^{eq} = \cos(\theta)\frac{1}{2}\left[ \frac{\partial F}{\partial B} - \frac{\partial (h_{em} + h_{ck})}{\partial \ln \kappa} \cdot \frac{\sin^2\theta (1 - \epsilon^2)}{\sqrt{\epsilon^2 \sin^2(\theta) + \cos^2(\theta)}} \right] , \tag{2.16}$$

and

$$H_r^{eq} = \sin(\theta)\frac{1}{2}\left[ \frac{\partial F}{\partial B} + \frac{\partial (h_{em} + h_{ck})}{\partial \ln \kappa} \cdot \frac{\cos^2\theta (1 - \epsilon^2)}{\sqrt{\epsilon^2 \sin^2(\theta) + \cos^2(\theta)}} \right] . \tag{2.17}$$

Here $\theta$ is the angle between $B$ and the crystal axes, $\epsilon$ is the anisotropy parameter and $h_{em}$ and $h_{ck}$ are the reduced values for $H_{em}$ and $H_{ck}$ from Eqs. [(2.9) and (2.10)] [15].

## 2.5 Surface barrier to flux entry

**Bean-Livingston surface barrier**

This section contains a brief summary of an investigation by C.P. Bean and J.D. Livingston [20] on the effect of a potential-energy barrier to the entry of flux at the surface of a Type II superconductor. A potential-energy barrier at the surface causes the entry of a vortex into the bulk to be delayed to field strengths above the lower critical field, $\boldsymbol{H}_{c1}$ and the exit of flux is similarly delayed until the external field has fallen below $\boldsymbol{H}_{c1}$. In their investigation, an elementary treatment of the interaction between a vortex and the specimen surface is considered. The nature of the surface barrier is explained with the aid of a simple physical picture using the method of images for the case where the external applied magnetic field is parallel to the surface as considered below. There are two separate forces which a vortex feels near the surface namely:

(1) A image of opposite polarity to the real vortex ensures a necessary boundary condition, namely, that the current normal to the surface is zero. There is then an attractive force between the vortex and its image. This attraction gives a contribution to the potential energy of the form:

$$V_A(x) = \frac{\Phi_0^2 K_0(2x/\lambda(T))}{\lambda^2(T)}\,, \tag{2.18}$$

where $K_0$ is a modified Bessel function of zero order.

(2) A external field $\boldsymbol{H}$ penetrates into the superconductor. If this field is of the same sign as the field of the vortex , this produces a repulsive force away from the surface into the superconductor, and a contribution to the potential, $V(x)$ of the form:

$$V_R(x) = -\Phi_0 H \exp\{-[x/\lambda(T)]\}\ . \tag{2.19}$$

The addition of these two contributions to the potentiel $V(x)$ gives a maximum value of the potential-energy near the surface for external magnetic fields below a certain threshold

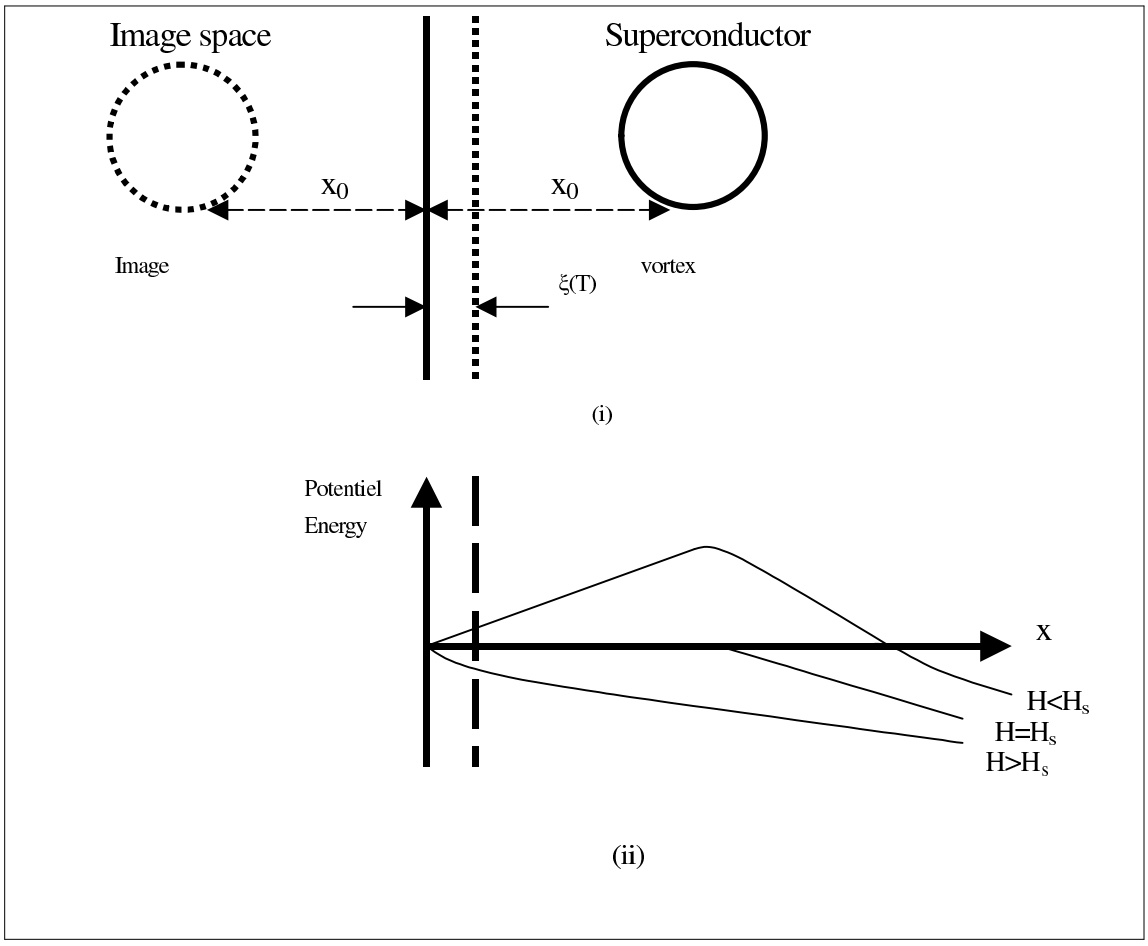


FIG. 2.2. Surface barrier to vortex entry.

value $\boldsymbol{H}_s$. This energy barrier to flux motion exists at only low fields i.e. for $\boldsymbol{H} \lesssim \boldsymbol{H}_c$. Without these surface effects, internal vortices become energetically favorable [21] at a lower critical field $\boldsymbol{H}_{c1}$. However, the presence of this surface energy barrier suggests that with a perfect surface, at absolute zero, vortices may not be able to enter until $\boldsymbol{H}_0 > \boldsymbol{H}_s$ at which field the barrier to flux penetration no longer exists. This effect is usually small, due to surface roughness on the scale of $\lambda$, and is usually insignificant in relation to the geometry-effect for platelet specimens. It will be ignored in the following.

# Chapter 3

# EXPERIMENTAL

## 3.1 Introduction

In this chapter, a general description of the vibrating sample magnetometer used for the $M_H$ measurements is given. We briefly discuss the characteristic features of the "high-$T_c$" superconducting oxides (BSSCO and YBCO) and present the magnetization measurements performed by Doyle *et al.* [22], for the disc specimen, Dewhurst *et al.* [23], for the platelet specimen and TB. Doyle for the YBCO specimen. These magnetization measurements are used in this work for fitting to the theoretical model.

## 3.2 Description of Experimental Method

### 3.2.1 Vibrating Sample Magnetometer

The first published design of a vibrating sample magnetometer is due to Foner [24]. The vibrating sample magnetometer uses an induction technique that consists in the detection of an AC emf induced by the vibration of a magnetic sample (in a uniform magnetic field) in a sense coil arrangement, i.e. by the mutual inductance of the coil and sample. Here we focus only on the basic operation of the magnetometer as shown in Fig. 3.1.

A mechanical transducer (TR) is driven at a fixed frequency $\nu$ of approximately 82Hz by an oscillator and power amplifier (A6). This causes the two annular capacitor plates (PV)

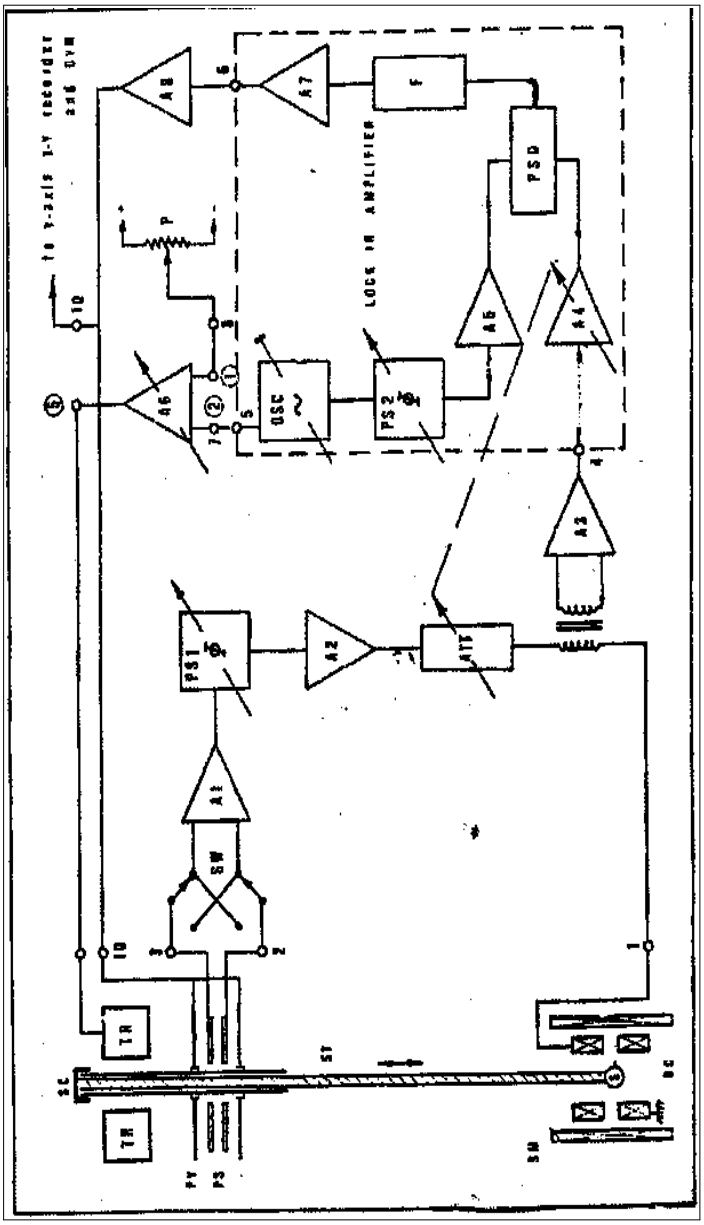


FIG. 3.1. Diagram of the electronics used in the vibrating-sample magnetometer [17].

and the specimen (S), which are mechanically coupled by a sample road (ST), to vibrate approximately synchronously with an amplitude of order 0.1-0.3 mm. While the specimen is vibrating in the solenoid SM, it sets up a time varying component of the field which induces a signal in the detection coils (DC) given by:

$$v_s(t) = \alpha\, a\, \nu\, m\, \cos(2\pi\nu t + \phi_s)\,, \tag{3.1}$$

where $\alpha$ is a geometrical constant relating to the coils (DC), $a$ is a the vibration amplitude, $\nu$ is the vibration frequency, $m$ is the magnetic moment of the specimen, and $\phi_s$ is the phase of the signal relative to the oscillator (OSC). If the product $a\,\nu$ remains constant, then $v_s = \text{const} \times m$. In practice, however, it is difficult to keep the vibration amplitude $a$ and the phase $\phi_s$ constant. This problem is solved by means of the phase-locked loop. Thus applying a DC potential, V , to the vibrating plates (PV), generates a signal on each of the two stationary plates (PS) of the capacitor, which is given by:

$$v_R(t) = \pm\,\beta\, a\, \nu\, v\, \cos((2\pi\nu\, t + \phi_R)\,, \tag{3.2}$$

where $\beta$ is a constant relating to the capacitor geometry and $\phi_R$ is the phase of the signal relative to the oscillator (OSC). It appears again that $v_R = \text{const} \times\ v$ only if the product $a\,\nu$ is constant. The reference signal, $v_R$, is passed through a series of amplifiers $A_1\,, A_2$ and an attenuator (AT). Its phase is adjusted with the aid of a switch (SW) and a phase shifter (PS1) in order to be almost identical with that of the signal $v_s$ for the detection coils.

The signal $v_R$ is then mixed with $v_S$ in the primary winding of the transformer T. The error signal $v_E$, across the secondary winding of the transformer T is then given by

$$v_E = v_S - G_1\, v_R\,, \tag{3.3}$$

where $G_1 = (Gain\, A_1) \times (Gain\, PS1) \times (Gain\, A_2) \times (Gain\, A_{TT})$. By adjusting the DC potential $v$ on the vibrating plates PV the error signal $v_R$ may be set approximately to zero. The magnetic moment $m$ is then obtained from Eqs. [(3.1), (3.2) and (3.3)], and is given by:

$$m = A\, v\,, \tag{3.4}$$

where $A = (G_1\, \beta/\alpha)$ is a constant. This null method therefore gives the magnetic moment directly in terms of the DC potential, $v$, independently of $a\nu$. In the automatic, phase-

locked loop mode, the error signal $v_E$ is amplified in a low noise amplifier $A_3$ and a tuned amplifier $A_4$, and then synchronously rectified in a phase sensitive detector P.S.D, (driven by the oscillator and amplifier $A_5$). The DC output of the P.S.D is passed through an adjustable low-pass filter, F, amplified by amplifiers $A_7$ and $A_8$, and finally applied to the vibrating plates PV. The output voltage from $A_8$ is in the range -30V$< v <$+30V and has the advantage of allowing the magnetic moment of the specimen to change the polarity without the necessity of changing the phase of the reference signal $v_R$ by using the switch, SW. From the foregoing it is clear that $v \propto |v_E|$, and the system is in equilibrium when

$$v = \gamma\,|(v_s - G_1\,v_R)| \times \mathrm{sign}(v_S - G_1\,v_R)\,, \tag{3.5}$$

where $\gamma$ is the loop gain of the detection systems, $v_S$ and $v_R$ are in phase with each other and are given by

$$v_S = \alpha\,a\,\nu\,m\,\cos(2\pi\nu t + \phi_S)\,, \tag{3.6}$$

and

$$v_R = \beta\,a\,\nu\,v\,\cos(2\pi\nu\,t + \phi_R)\,. \tag{3.7}$$

From Eq. (3.5), it can easily be shown that

$$v = \left[\frac{\gamma\,\alpha\,a\,\nu}{1 + G_1\,\gamma\,\beta\,a\,\nu}\right] m\,. \tag{3.8}$$

In the limit $G_1\,\gamma\,\beta\,a\,\nu \gg 1$, $m$ is given by

$$m \;\cong\; v\,(\frac{\beta\,G_1}{\alpha})\,, \tag{3.9}$$

and is independent of $a\nu$ as desired.

## 3.3 High-$T_c$ Superconducting Ceramic Oxides

### 3.3.1 Structure and Chemistry

Most high-$T_c$ superconductors (HTSC) have a perovskite structure $ABX_3$. This structure is cubic. With a few exceptions, HTSC are mainly cuprates i.e. compounds containing copper in their structure. A fully oxygenated unit cell of $Y_1Ba_2Cu_3O_{6+x}$ (YBCO), with $x = 1.0$, is shown in Fig. 3.2. The unit cell is orthorhombic with lattice parameters of $a$ ~4Å and $c$ ~12Å. The superconducting carriers (holes) are known to be located predominantly in the $CuO_2$ planes. Consequently $Y_1Ba_2Cu_3O_{6+x}$ exhibits superconducting properties that are highly anisotropic. The preferred current conducting direction is in the a-b (basal) plane, with the c-axis direction being relatively more weakly conducting [25].

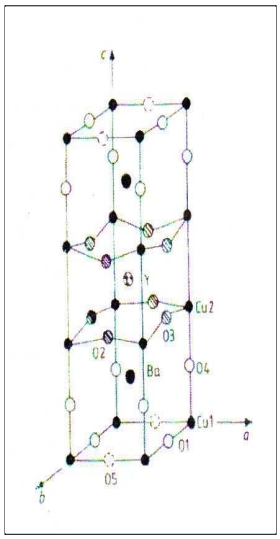


FIG. 3.2. Unit cell for Superconducting $Y_1Ba_2Cu_3O_{6+x}$ (x=1.0) [2].

The partial "oxygen content", $x$, in the formula $Y_1Ba_2Cu_3O_{6+x}$ determines the hole concentration in the $CuO_2$ planes. A non-superconducting tetragonal phase occurs for $0.0 < x < 4.0$ while a superconducting orthorhombic phase is obtained for $0.4 < x < 1.0$. When oxygen is diffused into the oxygen deficient $Y_1Ba_2Cu_3O_{6+x}$ the oxygen goes into vacancy sites in the parallel Cu-O chains (along the b axis of Fig. 3.2). In order to maintain a net zero charge, electrons are removed from the $CuO_2$ planes, thereby creating "conduction" holes in the $CuO_2$ planes that are available to form Cooper-pairs when $T < T_c$. The valence or charge state of the Cu atoms depend on the partial oxygen content. For example

$Y_1Ba_2Cu_3O_6$, an insulator, contains $Cu^{2+}$ ions in the $CuO_2$ planes and $Cu^{3+}$ ions in the Cu-O chains, while $Y_1Ba_2Cu_3O_7$ a superconductor, contains $Cu^{2.33+}$ ions [26] (assuming that charge is distributed equally between the Cu atoms).

### 3.3.2 High Critical Temperature

High-$T_c$ materials possess critical temperatures that far exceed the BCS limit, extending beyond 150K [9] for certain systems. However, as we said in chapter 2, the mechanism for high-$T_c$ superconducting materials is not yet fully understood. The onset critical temperatures $T_c$ for YBCO and BSCCO (disc and platelet), which are materials used in the present investigation, are respectively approximately 93K and 85K [22] and 85.3K [23]. The binding energy of the Cooper-pairs, $\triangle(0)$, is approximately 10meV at 100K. This value is about ten times greater than the binding energy of the Cooper-pairs in conventional superconductors, implying that the Cooper-pairs are more tightly bound in ceramic superconductors.

### 3.3.3 Short Coherence Length

The high-$T_c$ materials (especially cuprates [25]) have very short coherence lengths ($\xi$ is of the order of and less than 10Å). This is expected from the BCS theory, which predicts $\xi \propto T_c^{-1}$. For the YBCO: $\xi_{ab}(0)\sim$15Å and $\xi_c(0)\sim$4Å with $\lambda_{ab}(0)\sim$ 1500Å and $\lambda_c(0)\sim$6000Å. Thus $\kappa_{ab}$ / $\xi_{ab}$ $\simeq 100 \gg 1$, and YBCO is an extreme Type II superconductor. This short coherence length, of the order of the dimension of a unit cell, is partly responsible for the granular effect associated with these systems.

### 3.3.4 Specimens preparation

Polycrystalline specimens of high-$T_c$ superconductors are prepared using a technique called **powder processing**. This technique includes a process called sintering, in which randomly oriented grains of the precursor material are effectively fused together. Generally, a floating zone technique is used for preparation of the $Bi_2Sr_2CaCu_2O_{8+\delta}$ single crystal material. This technique is advantageous because it allows for the production of high quality sin-

gle crystals whilst overcoming the problems encountered in growing single crystals from compounds which melt incongruently. The traveling floating zone technique is successful in producing boules containing large single crystals of high temperature superconductors such as $La_{1.85}Sr_{0.15}CuO_4$ and $Bi_2Sr_2CaCu_2O_{8+\delta}$. The sample temperature can be controlled with a camera allowing direct observation of the melting and crystallization processes [27].

**Procedure for the Disc and Platelet BSCCO Specimen**

A single crystal sample of over-doped BSCCO with $T_c = 85$K was grown using an infrared floating furnace [28]. This boule was cleaved to yield a single crystal with optically smooth parallel surfaces and thickness d = 0.01 ± 0.002 mm. This crystal was gently mechanically polished, into a disk with $R = 0.5 \pm 0.001$ mm with the c-axis normal to the large surfaces [22]. For the platelet specimen, a sample of BSCCO was grown using a traveling floating zone technique in a double ellipsoidal infrared furnace [29], which produced a mosaic of large aligned crystallines. This mosaic was repeatedly cleaved until a single optically smooth crystal was obtained with dimensions of 0.6 mm x 1.7 mm and thickness of 15 mm [23].

**Procedure for the Platelet YBCO Specimen**

For the YBCO, particle size of a few $\mu$m are required and work done on YBCO indicate that favorable sintering temperatures range between $925^0$ C and $950^0$ C (for several hours) [30, 31]. After repeated grinding and calcining, the specimen used had the approximate dimensions: Length: $L = 1.27$ x $10^3$ $\mu$m, Aspect ratio: $W/t = 8.4$, Width: $W = 0.76$ x $10^3$ $\mu$m, Volume: $V = 87.35$ x $10^{-6}$cm$^3$, Thickness $t = 90.5$ $\mu$m.

## 3.4 Magnetization Measurements

### 3.4.1 BSCCO single crystals

Isothermal D.C magnetization measurements were performed on BSCCO single crystals with the magnetic field applied parallel to the c-axis for the disc specimen by Doyle *et al* [22] and for the platelet by Dewhurst *et al* [23]. $M - H_0$ hysteresis loops for various temperatures in the range 30K $\leq T \leq$ 70K for the disc specimen are given in Fig. 3.3. The $M - H_0$ data at $T$ =30K shows the arrow-head effect which occurs at the dimensional cross-over from 3D to quasi 2D behavior [23, 32]. The $M - H_0$ data at $T = 40$K shows the step-effect or magnetic-jump which has been associated with a vortex lattice solid/liquid melting transition [33, 34].

Fig. 3.4. gives $M - H_0$ hysteresis loops for various temperatures in the range 30K $\leq T \leq$ 70K for the platelet specimen. A small amount of hysteresis is present at low fields but the magnetization loops become reversible at the irreversibility field, $H_{irr}$. A broad melting step and change in slope of the reversible magnetization is just visible in the data and is marked on the figure at the melting field, $H_m$ close to where the loops become reversible [23].

### 3.4.2 YBCO single crystal

Measurements were done on a SQUID magnetometer at the IRC for superconductivity, University of Cambridge (by T.B Doyle). $M - H_0$ hysteresis loops for various temperatures in the range 85K$\leq T \leq 92K$ for the YBCO specimen are given in Fig. 3.5.

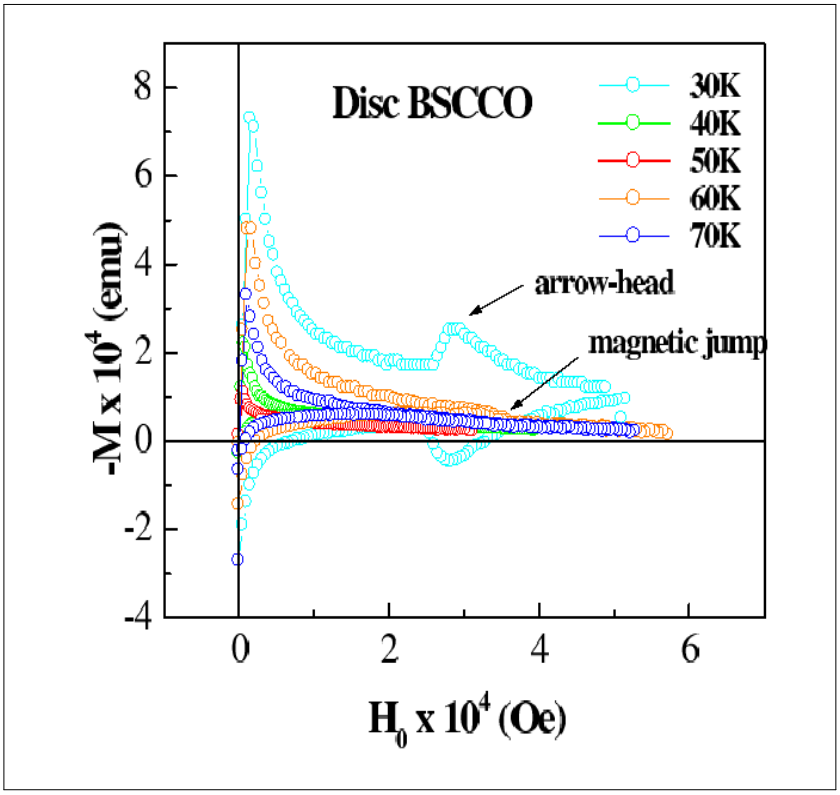


FIG. 3.3. Isothermal d.c. magnetization ($M - H_o$) curves for the BSSCO disc specimen for $30K \leq T \leq 70K$ [22].

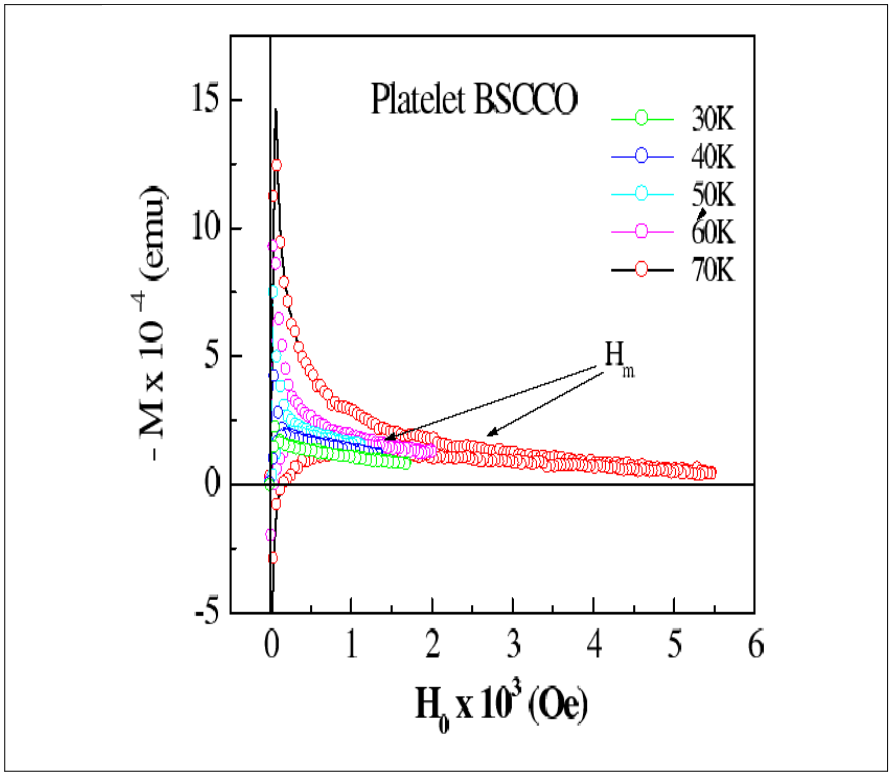


FIG. 3.4. Isothermal d.c. magnetization ($M - H_o$) curves for the BSSCO platelet specimen for $30K \leq T \leq 70K$ [23].

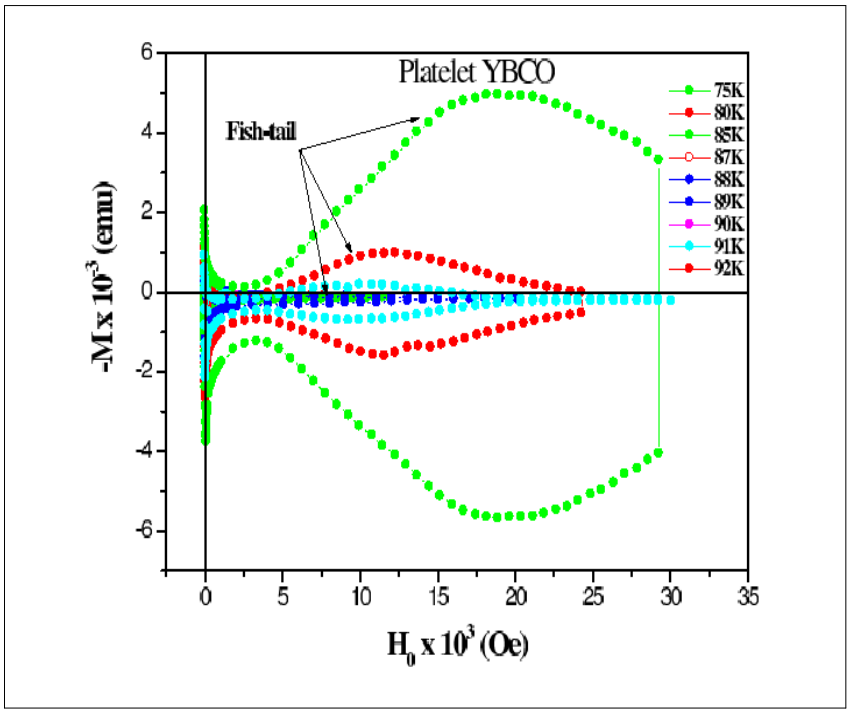


FIG. 3.5. Isothermal d.c. magnetization $(M - H_0)$ for the YBCO specimen, for $75K \leq T \leq 92K$.

# Chapter 4

# RESULTS AND DISCUSSION

## 4.1 Theory and numerical computation

The theoretical model used in this work to obtain the quasi-static current density and internal field profiles, and hence also the $\boldsymbol{M}(\boldsymbol{H}_o)$ behavior, has been developed by Doyle and Labusch [18, 19]. This treatment allows for the inclusion of explicit expressions for the constitutional equilibrium $\boldsymbol{B}^{rev}(\boldsymbol{H})$ relation in the solid and liquid vortex phases, for vortex pinning and for a discontinuous (first-order) melting phase transition at any chosen local field value. The basic equations which include the magnetic boundary conditions for this treatment have been summarized in section 2.3 and represented specifically in Eqs. [(2.1)-(2.4)], namely,

$$\Delta G = \Phi_0 \int (\boldsymbol{H}^{rev} - \boldsymbol{H}^e) \cdot d\boldsymbol{l}\,, \tag{4.1}$$

$$\sigma(\boldsymbol{r}_s) = H^e_\perp - B_\perp/4\pi\,, \tag{4.2}$$

$$\boldsymbol{H}^e(\boldsymbol{r}) = \boldsymbol{H}_0 + \frac{1}{4\pi}\iint \frac{\sigma(\boldsymbol{r}_s)(\boldsymbol{r}-\boldsymbol{r}_s)d^2\boldsymbol{r}_s}{|\boldsymbol{r}-\boldsymbol{r}_s|^3}\,, \tag{4.3}$$

and

$$\boldsymbol{f} = \Phi_0[(\boldsymbol{\nabla}\times\boldsymbol{H}^{rev})\times\boldsymbol{B}]\times\boldsymbol{B}/B^2 + \boldsymbol{f}_p\,. \tag{4.4}$$

The method of iterative numerical solution and the assumptions used to solve these equations are summarized below.

A circular flat disc specimen of isotropic material of radius $R$ and thickness $d$ is placed in a perpendicular field $\boldsymbol{H}_o$. In cylindrical co-ordinates $(r, z, \varphi)$, it feels a field $\boldsymbol{H}_o = (0, 0, H_o)$ and it flats surfaces are at $z = \pm\, d/2$. The analysis can be simplified by assuming that at a distance $r = R(z)$ the outer surface of the disc is barrel shaped in such a manner that it is everywhere parallel to $\boldsymbol{H}^e$. The charges on the cylindrical perimeter surface can then be neglected and the boundary condition on this surface may be written as:

$$\boldsymbol{H}^{rev}(\boldsymbol{B}(R)) = \boldsymbol{H}^e(R)\,. \tag{4.5}$$

Elementary calculus of Eq. (4.2) and Eq. (4.3) gives the values for $\boldsymbol{H}^e$, $\boldsymbol{H}^{rev}$ and $\boldsymbol{B}$ at $z = d/2$ and represented by the following expressions:

$$\sigma(r) = H_z^e(r, d/2) - B_z(r, d/2)/4\pi\,. \tag{4.6}$$

$$H_z^e(r, d/2) = H_0 + \frac{\sigma(r)}{2} + \frac{1}{4\pi} \times \int_0^R \int_0^{2\pi} \frac{\sigma(r')\, r'\, d}{\left(d^2 + r^2 + r'^2 - 2r\, r' \cos\varphi\right)^{3/2}} dr'\, d\varphi\,, \tag{4.7}$$

and

$$H_r^e(r, d/2) = \frac{1}{4\pi} \int_0^R \int_0^{2\pi} \sigma(r')(r - r'\,\cos\varphi) r' \times \left[ \frac{1}{\left(r^2 + r'^2 - 2r\, r'\,\cos\varphi\right)^{3/2}} - \frac{1}{\left(d^2 + r^2 + r'^2 - 2r\, r'\,\cos\varphi\right)^{3/2}} \right] dr'\, d\,\varphi \tag{4.8}$$

The values at $z = -\,d/2$ are obtained from symmetry. At the surface $H_{\|}^{rev} = H^{rev} = H_{\|}^e$, $H_r^{rev} = (B_r/B) H^{rev}(B)$ and $B_r = \sqrt{B^2 - B_z^2}$. Applying the boundary condition at $z = d/2$,

$$H_r^e = \sqrt{(B^2 - B_z^2)}\, H^{rev}(B)/B\,. \tag{4.9}$$

The solution of Eq. (4.4) within the boundary condition $H_{\|}^{rev} = H_r^e$ and using the relation $\mathrm{d}H_r^e/\mathrm{d}z = \mathrm{d}H_z^e/\mathrm{d}r$ (from $\boldsymbol{\nabla} \times \boldsymbol{H}^e = 0$) gives:

$$\boldsymbol{f} = \Phi_0 \left[ \frac{\mathrm{d}\boldsymbol{H}_z^e}{\mathrm{d}r} - \frac{\mathrm{d}\boldsymbol{H}_z^{rev}}{\mathrm{d}r} \right]_{z=d/2} + \boldsymbol{f}_p\,. \tag{4.10}$$

### Critical state

The critical state is obtained from Eqs. [(4.5) - (4.10)] which are solved simultaneously using a procedure that starts with an educated guess for the initial flux distribution profile $B_z(r, d/2)$, $H_z^e(r, d/2)$, and $H_0$ in the disc. In this process the result obtained for the surface charge density $\sigma(r)$ Eq. (4.6) is used to obtain the new values for $H_z^e(r, d/2)$ and $H_r^e(r, d/2)$ from Eqs. (4.7) and (4.8) respectively. The total force is then obtained from Eq. (4.10) by using $H_z^{rev} = (B_z/B)H^{rev}(B)$ where $B(r, d/2)$ has been re-evaluated from Eq. (4.9) and may be expressed as:

$$\boldsymbol{f} = \Phi_0 \left[ 2\frac{\boldsymbol{H}_r^e(r, d/2)}{d} - \frac{\partial \boldsymbol{H}^{rev}(\bar{B})}{\partial r} \right] + \boldsymbol{f}_p \,. \tag{4.11}$$

The first term and the second term in the square brackets of Eq. (4.11) gives respectively the absolute vortex curvature and vortex density gradient contributions to the driving force.

### Meissner regime and field of initial vortex penetration $H^p$

In order to obtain the reduced internal fields and the mean reduced internal fields, the boundary conditions are applied to the planar surfaces of the disc, with $\boldsymbol{B} = 0$. The contribution of extrinsic vortex pinning is ignored as we consider only the reversible regime of the magnetization isotherms. Numerical solutions of Eqs. [(4.5) - (4.8)] yields the internal fields, $\Phi_z(\rho\,, \zeta = \pm 1/2) \equiv H_z^e(\rho\,, \pm 1/2)/H_0$, $\Phi_z(\rho\,, 0)$ and the mean reduced internal fields;

$$\Phi_z^m(\rho) \equiv \frac{1}{H_0} \int_{-1/2}^{+1/2} H_z^e(\rho\,, \varsigma)\, d\varsigma \,,$$

and

$$\Phi_r^m(\rho) \equiv \frac{1}{H_0} \int_{-1/2}^{+1/2} H_r^e(\rho\,, \varsigma)\, d\varsigma \,,$$

where $\rho \equiv r/R$ and $\zeta \equiv z/d$. Fig. 4.1 shows plots of $z$-component of the reduced 'thermodynamic' fields at the top and bottom surfaces of the disc, $\Phi_z(\rho\,, \pm 1)$, and the mean, reduced, $z$-and radial $r$-components, $\Phi_z^m(\rho)$ and $\Phi_r^m(\rho)$ for various values of the aspect ratio $2R/d > 0$. We can see that $\Phi_z(\rho)$ decreases as $\rho$ increases.

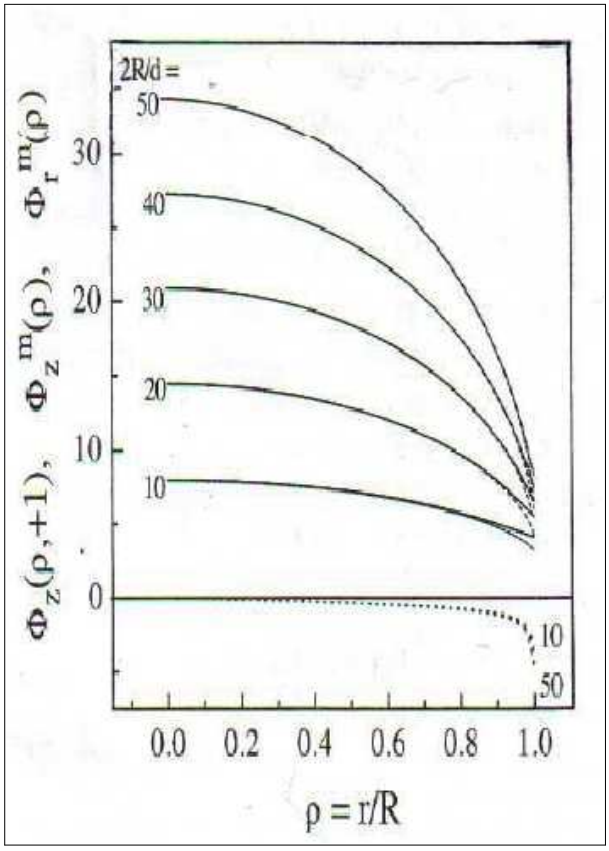


FIG. 4.1. Calculated reduced field profiles $\Phi_z(\rho\,,\pm 1)$, (solid curves), $\Phi_z^m(\rho)$ (dashed curves) and $\Phi_r^m(\rho)$ (dotted curves) in the Meissner state for various specimen aspect ratios $2\,R/d$ as indicated [19].

In transverse applied field $\boldsymbol{H}_0$ initial vortex penetration takes place across the sharp rims of the disc, where the local field intensity is much larger than the applied field. As the applied field $\boldsymbol{H}_0$ increases, at a certain critical value the leading adjacent vortex segments will join at the equatorial plane ($\rho = \rho_c$, $\zeta = \pm 1/2$) and ($\rho = 1\,, \zeta = 0$). In the absence of strong pinning forces these segments then join and the combined vortex rapidly straightens and is driven to the centre of the specimen by the potential gradient. Assuming that the leading vortex segments (vortices) across the rims are straight, and using the relation $\boldsymbol{\nabla} \times \boldsymbol{H}^e = 0$, Eq. (4.1) with $\boldsymbol{H}^{rev} = \boldsymbol{H}_{c1}$ can be written as:

$$\delta G = \frac{H_{c1}\Phi_0 d}{4\pi}\left[\sqrt{1 + (2\,\Delta\,\rho_c\,R/d)^2} - h\,\Phi_z^m(\rho_c)\right]\,, \tag{4.12}$$

where $h \equiv H_0/H_{c1}$ and $\Delta\rho_c \equiv 1 - \rho_c$. The minimum value of $h$, with respect to variation

in $\rho_c$ is the critical reduced applied field $h^p$ and is given by:

$$h^p = \left[\sqrt{1 + (2\,\Delta\,\rho_c\,R/d)^2}/\Phi_z^m(\rho_c)\right]_{\min} . \tag{4.13}$$

The accuracy of the present treatment depends on the precision of the $\boldsymbol{B}[\boldsymbol{H}^{rev}]$ relation used in the calculation. In order to simplify numerical calculation, the disc and the platelet specimens were treated as discs. All field vector quantities are parallel to the applied field $\boldsymbol{H}_0$, and hence also to the c-axes of the present crystal specimens. In this earlier work the heuristic expression Eq. (2.5) for the inverse $\boldsymbol{B}[\boldsymbol{H}^{rev}]$ relation was used and the calculated $M - H_0$ results as a function of $\boldsymbol{H}_0/\boldsymbol{H}_{c1}$, for ideal (i.e., with $\boldsymbol{f}_p = 0$) disc specimens of various aspect ratio $2\,R/d$, are represented in Fig. 4.2.

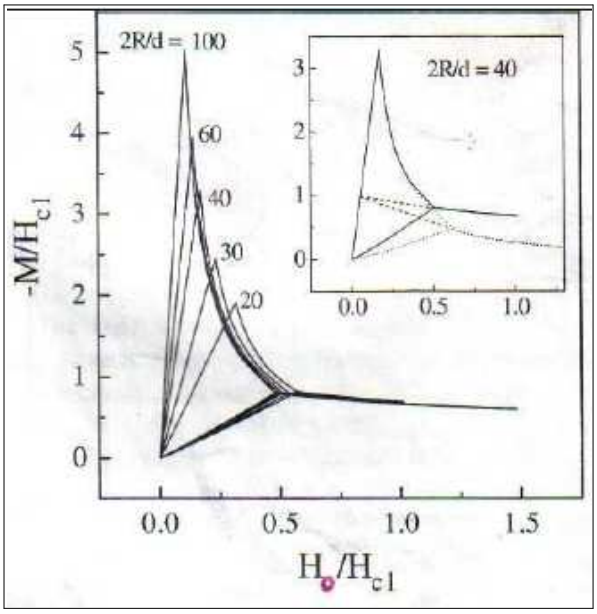


FIG. 4.2. Calculated reduced $\boldsymbol{M}(\boldsymbol{H}_0)$ curves for reversible $J_c = 0$ specimens with $\kappa = 70$ for various specimen aspect ratio $2\,R/d$, as indicated. The inset compares calculations for $\kappa = 70$ (solid curve) and for $\kappa = 0.79$ (dotted curve) in discs with $2\,R/d = 40$. The dashed curves show the equilibrium behaviour in the absence of the geometry effect [19].

In the inset in Fig. 4.2 are compared the behavior for $\kappa = 70$ (solid curve) and for $\kappa = 0.79$ (dotted-curve) for disc-specimens with $2\,R/d = 40$. The dashed curves shows the equilibrium behavior expected for an equivalent ellipsoid normalized to the same volume. From these results, it appears that there is a delay in the applied field for initial vortex penetration and a geometry-effect.

For the purpose of this work, we use a computer programme that incorporates the above treatment and that includes a routine for the calculation of the equilibrium constitutive $\boldsymbol{B}[\boldsymbol{H}^{rev}]$ from a solution of the Ginsburg-Landau equation for $\kappa \geq 1/2$ in uniaxial anisotropic materials [15]. In the theoretical derivations and the numerical algorithm, all field and magnetization values are normalized by $H_{c1}(T)$, which in the present treatment, together with $\kappa$, are treated as free fitting parameters.

## 4.2 Comparison with experiment

In order to compare the theoretical results and the experimental data, we proceeded as follow: as the calculated results were normalized by $H_{c1}$, the raw experimental $M - H_0$ isotherms for each specimen geometry were also normalized by $H_{c1}$. The next step was to find the mean $M$ (which approximates the reversible) normalized magnetization, $M\ /2H_{c1}$ $= (M_u + M_d)\ /2H_{c1}$ where u and d refer to the branches for increasing and decreasing $H_0$ over the entire $M(H_0)$ loop. The mean normalized magnetization were obtained from Fig. 3.3, Fig. 3.4 and Fig. 3.5 and are represented below:

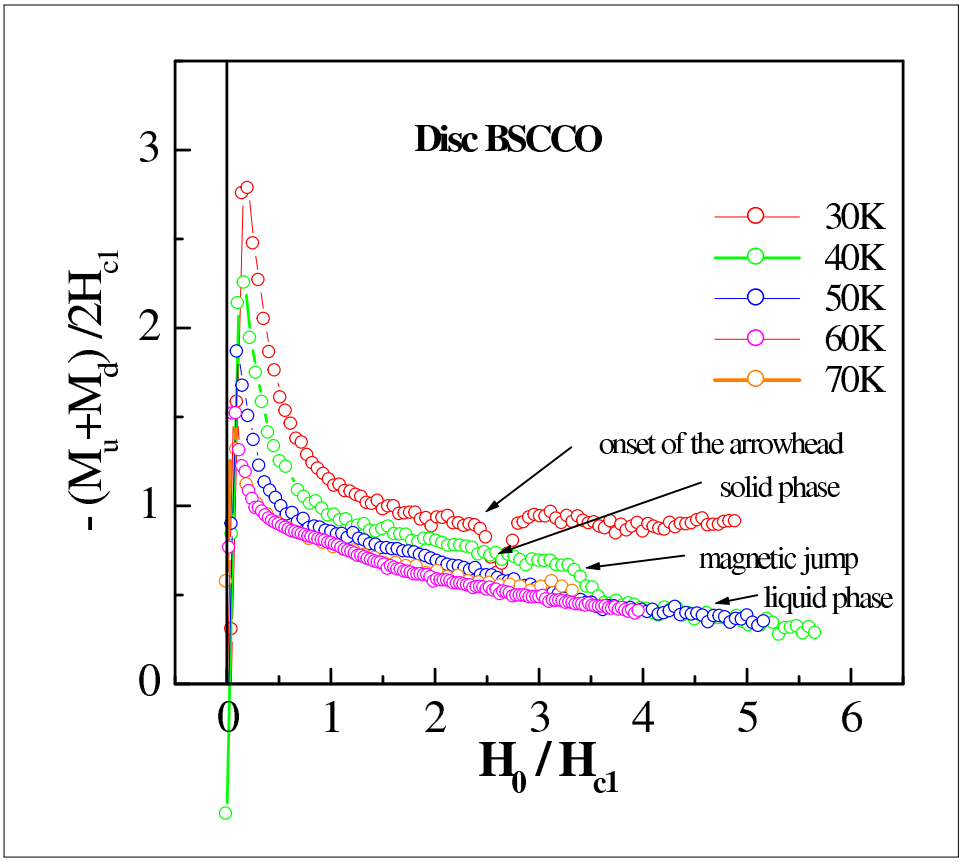


FIG. 4.3. Isothermal d.c.'mean' magnetization ($\overline{M} - H_0$) for the BSCCO disc specimen, for $30K \leq T \leq 70K$.

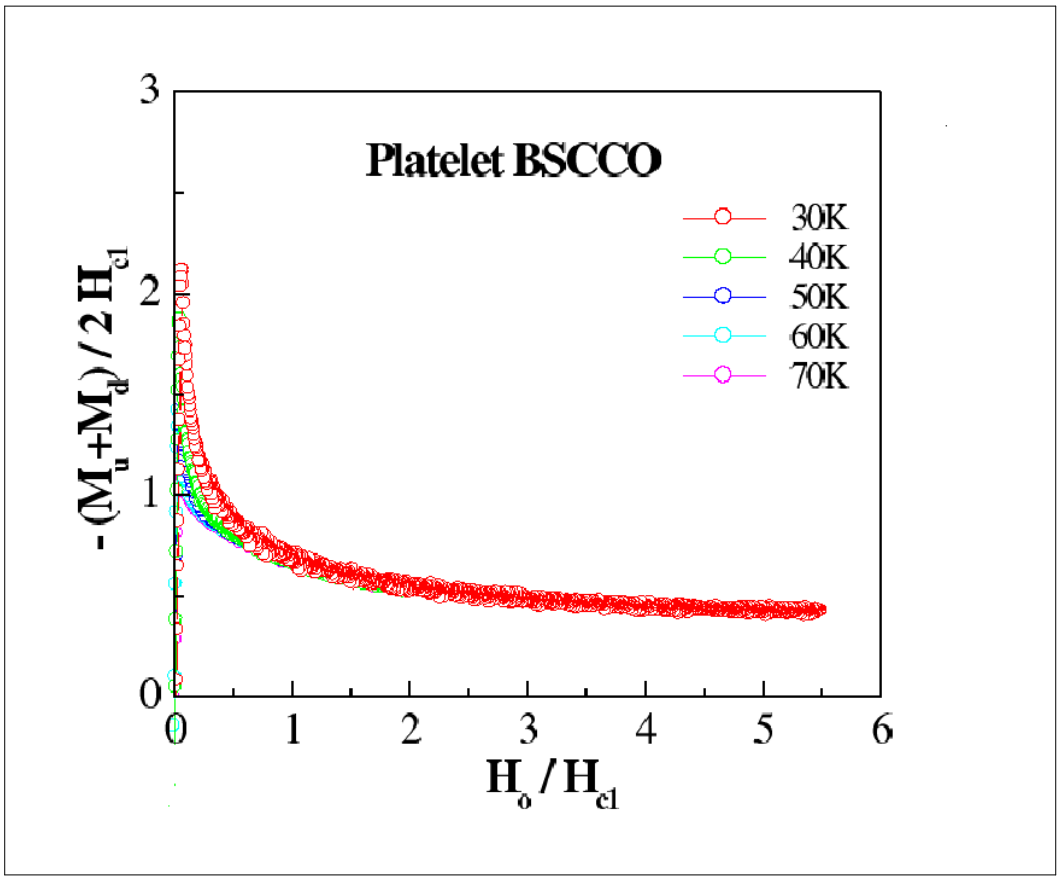


FIG. 4.4. Isothermal d.c. 'mean' magnetization $(\overline{M} - H_0)$ for the BSCCO platelet specimen, for $30K \leq T \leq 70K$.

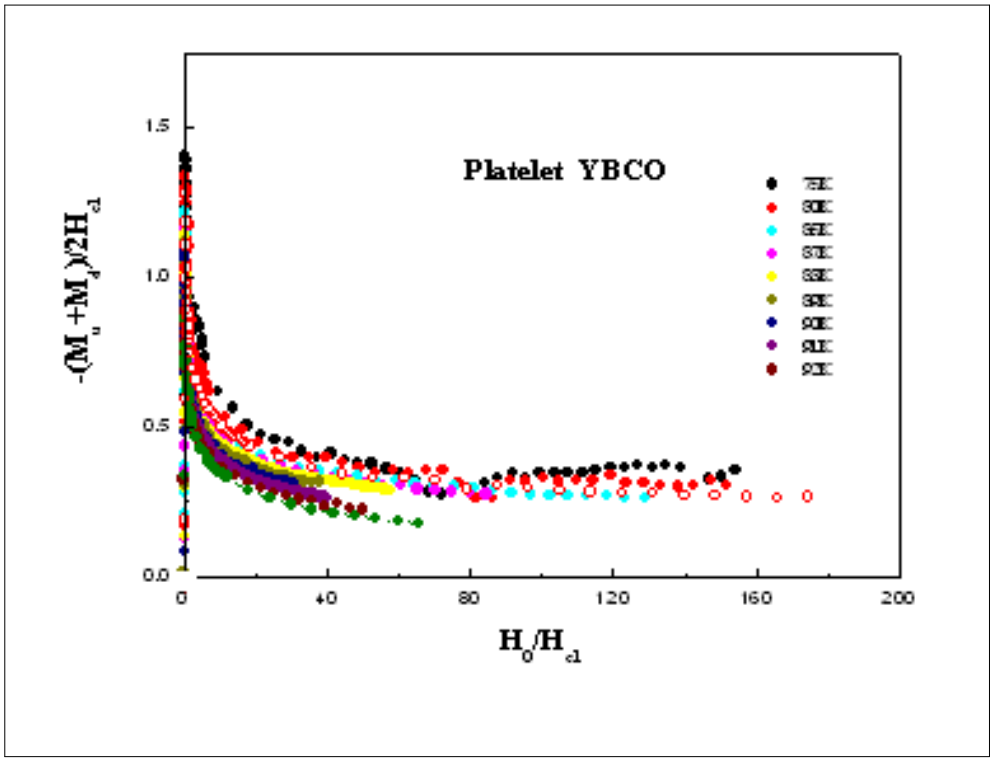


FIG. 4.5. Isothermal d.c. 'mean' magnetization ($\overline{M} - H_0$) for the YBCO specimen, for $75K \leq T \leq 92K$.

Consider first the results for the disc specimen, it will be noted from Fig. 4.3, that the " mean" $m-h$ normalized isotherms manifest a very pronounced solid/liquid vortex matter melting transition at $H_0/H_{c1} \simeq 3$ and show that there appear to be three different constitutive behaviors. The isotherm at ($T = 30$K) manifests the arrowhead phenomenon which is associated with a transition from solid to a "glass" vortex lattice. All $m-h$ curves for $T > 40$K tend to liquid phase as $H_0/H_{c1}$ increases. For the platelet specimen, the "mean" normalized $m-h$ isotherms become coincident and show no distinct solid/liquid vortex lattice transition Fig. 4.4. Once we obtained the mean magnetization ($m-h_0$) we proceeded as explained below.

### 4.2.1 Procedure for the disc BSCCO Specimen

The calculated $m^{rev}(h_0)$ curve was computed in the programme where $\kappa$ was fixed at a value of 70 which is the known approximate value [11] and has been fitted to the solid crystalline behavior. The $m^{rev}(h_0)$ curve extrapolates to $m^{rev}(h_0) = 1$ with a gradient of unity as $m^{rev}(h_0) \longmapsto 1$ yields the result $f(T) = H_{c1}(T)$. After the initial values for $\kappa$ and $H_{c1}$ have been obtained, we change the values of these parameters until the theoretical curve fits exactly the experimental isotherm. When we reach this point we record the values of the two fitting parameters $\kappa$ and $H_{c1}$ and we proceed the same for all isotherms at different temperatures. The value of $\kappa$ for the "liquid" phase was $\kappa = 3$ and for the arrowhead regime $\kappa = 250$. Note that we only found the parameters $\kappa$ and $H_{c1}$ and we deem our fit acceptable if the experimental data and model looks good, (chi-by-eye approach). In Fig. 4.6 are shown the theoretical fits to the "mean" experimentally determined magnetization isotherms. The "mean" experimental magnetization isotherms are represented in open symbol while the solid, dashed, and dotted curves are the calculated equilibrium behavior for the liquid, solid crystalline, and the arrowhead regime, respectively. For the sake of clarity we represent each fit in the regime of the arrowhead i.e. at 30K, fully solid at 40K and fully liquid for $T \geq 70$K, in Figs. 4.7- 4.9, respectively.

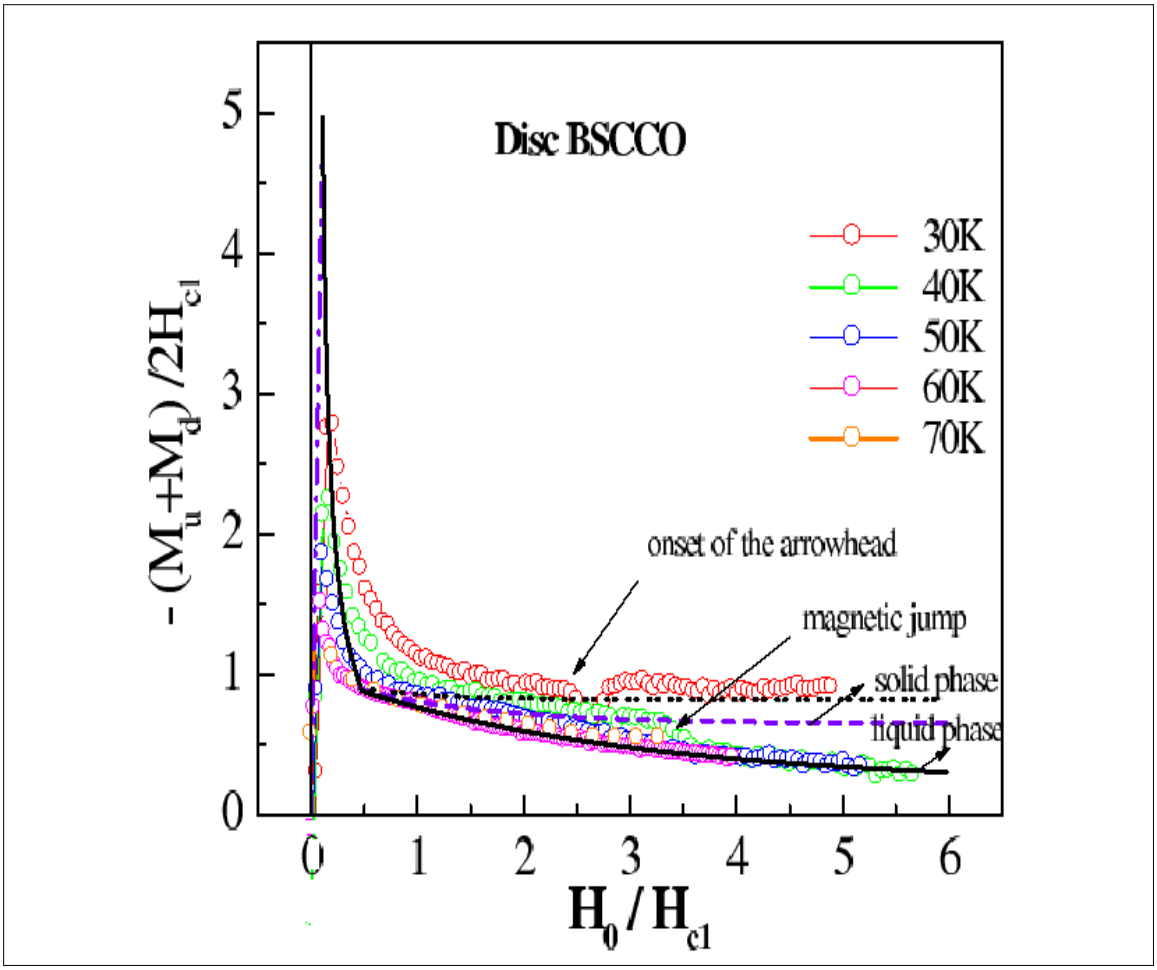


FIG. 4.6. Normalized 'mean' magnetization isotherms for the disc specimen.

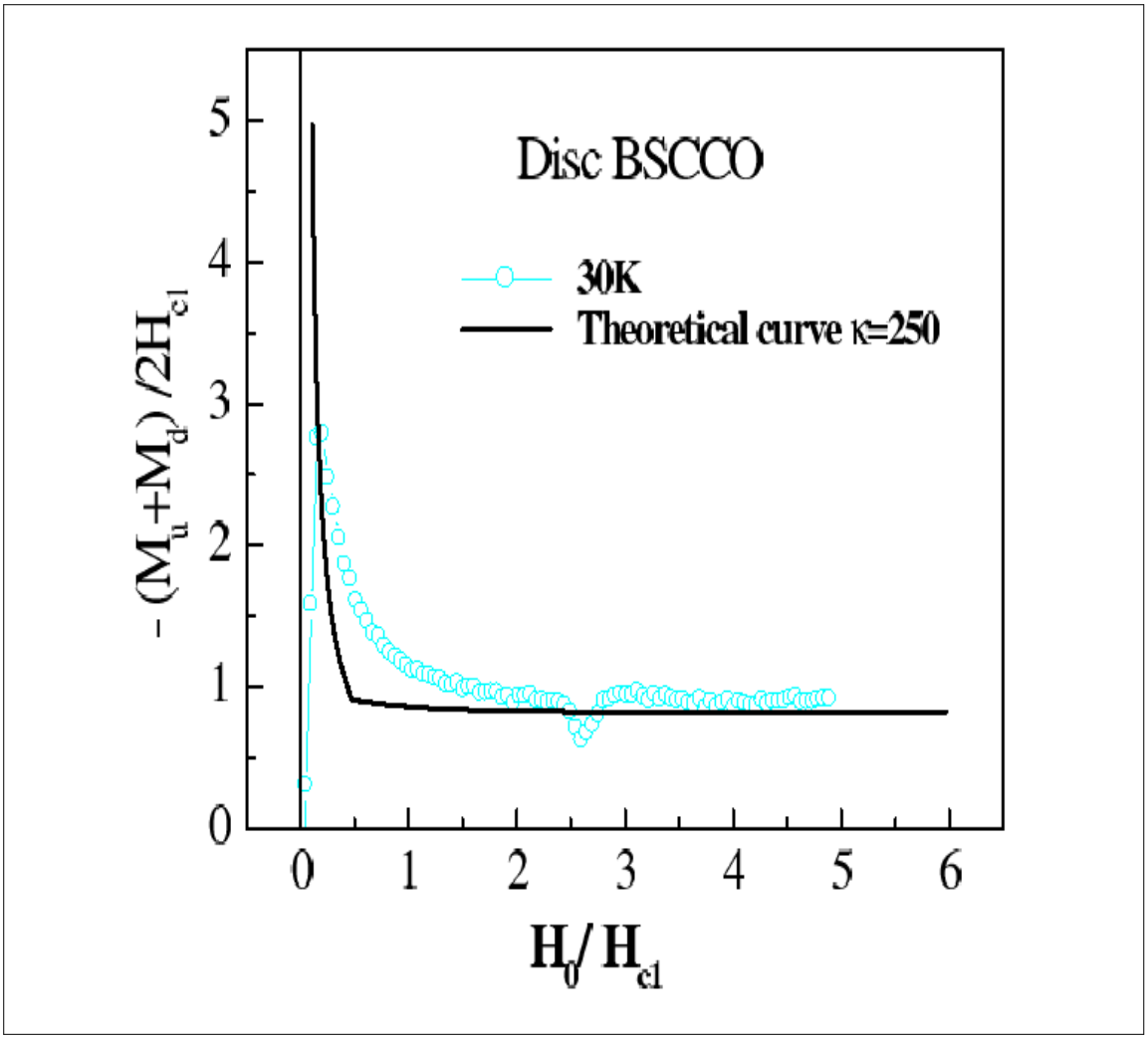


FIG. 4.7. Theoretical fit (solid curve) to experimental ($\overline{M} - H_0$) isotherm for the arrowhead regime, i.e. $T$=30K.

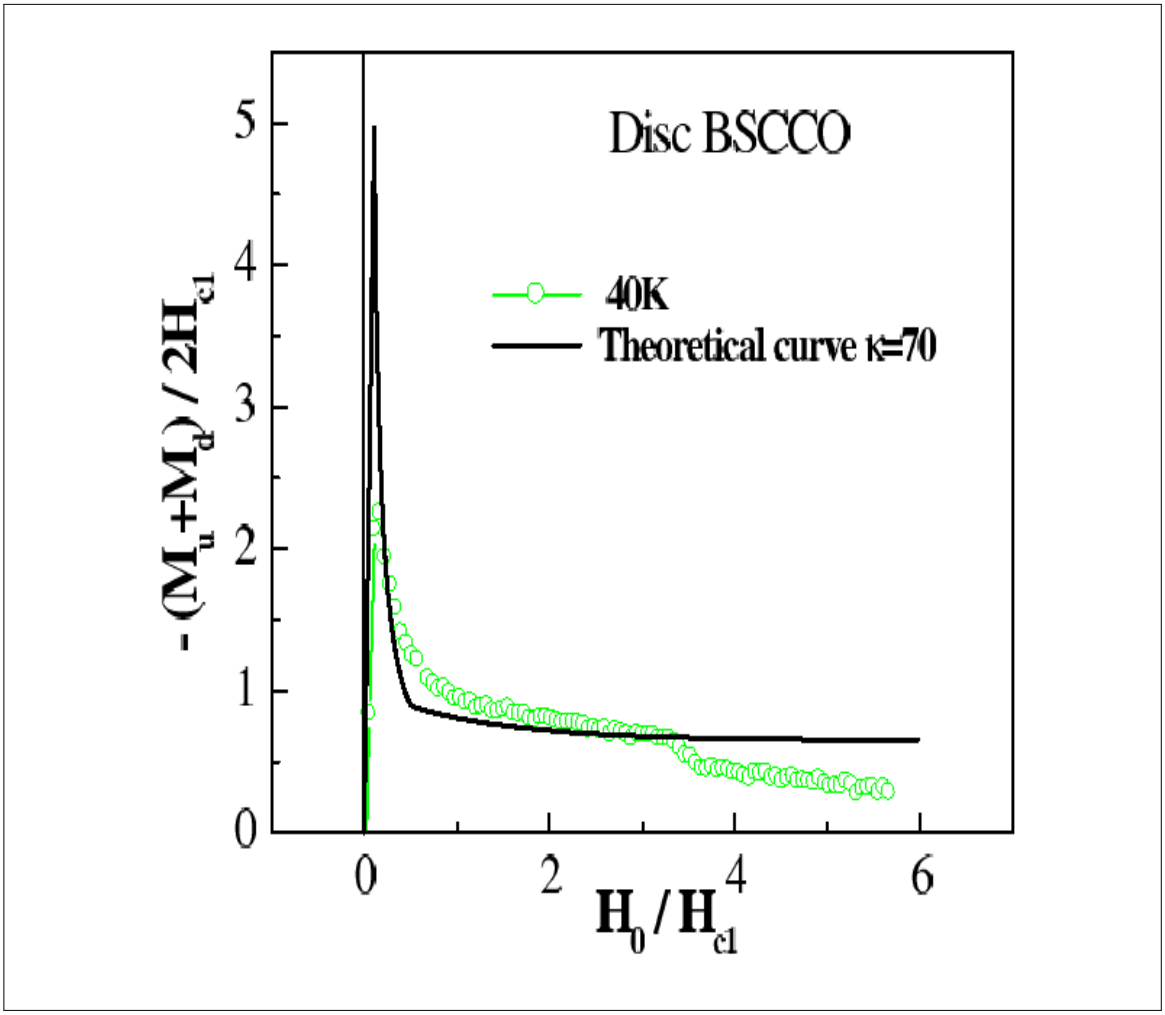


FIG. 4.8. Theoretical fit (solid curve) to experimental $(\overline{M} - H_0)$, isotherm for the fully solid phase, i.e. $T$=40K.

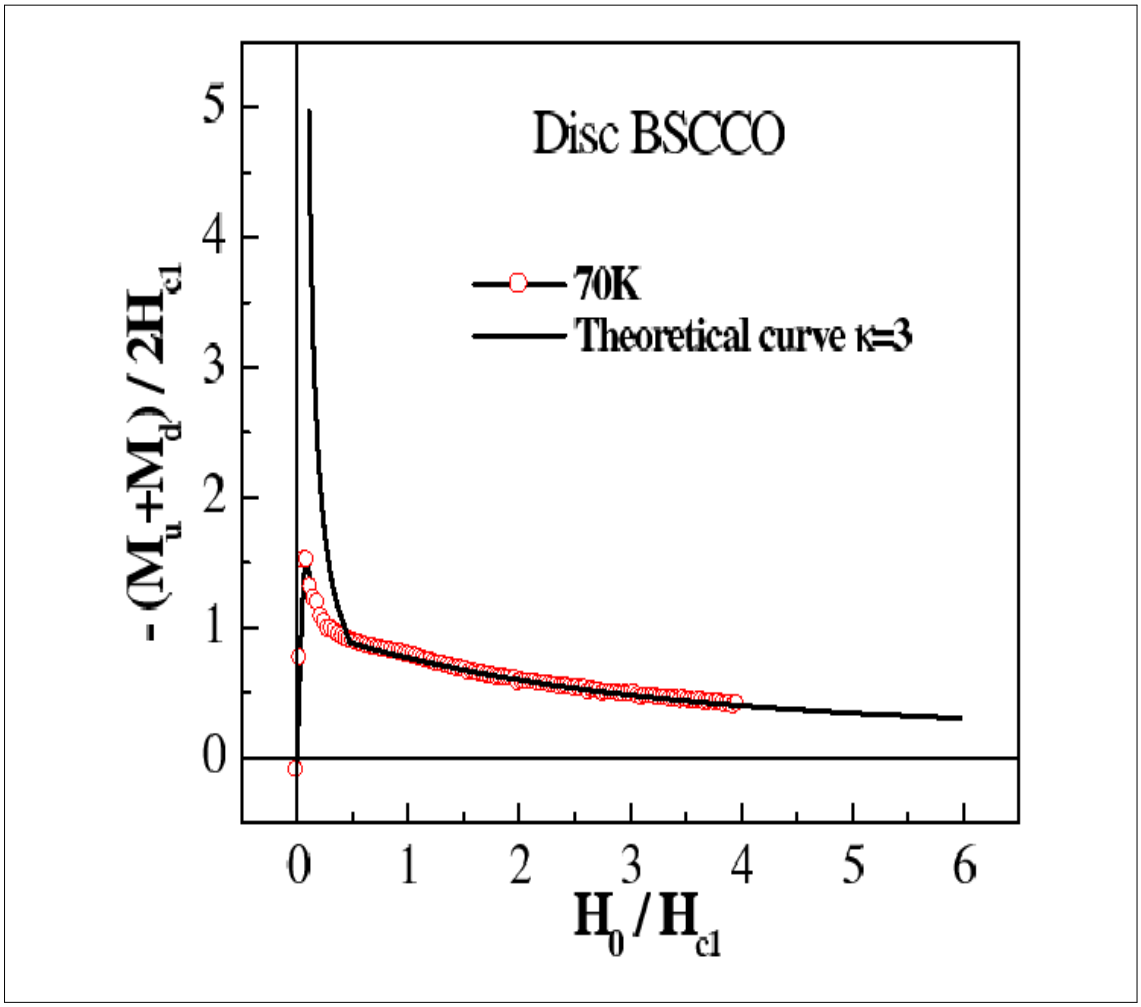


FIG. 4.9. Theoretical fit (solid curve)to experimental $(\overline{M} - H_0)$, isotherm for the fully liquid phase, i.e. $T \leq 70K$.

### 4.2.2 Procedure for the platelet BSCCO Specimen

As the platelet BSSCO specimen, of different oxygen stoichiometry showed no distinct solid/liquid vortex lattice transition, the calculated $m^{rev}(h_0)$ curve with $\kappa = 70$ was fitted over the entire $(B - T)$ plane. In Fig.4.10 we show the results for the platelet specimen. The calculated solid phase is in solid curve while the open symbols represent the normalized 'mean' experimental magnetization isotherms.

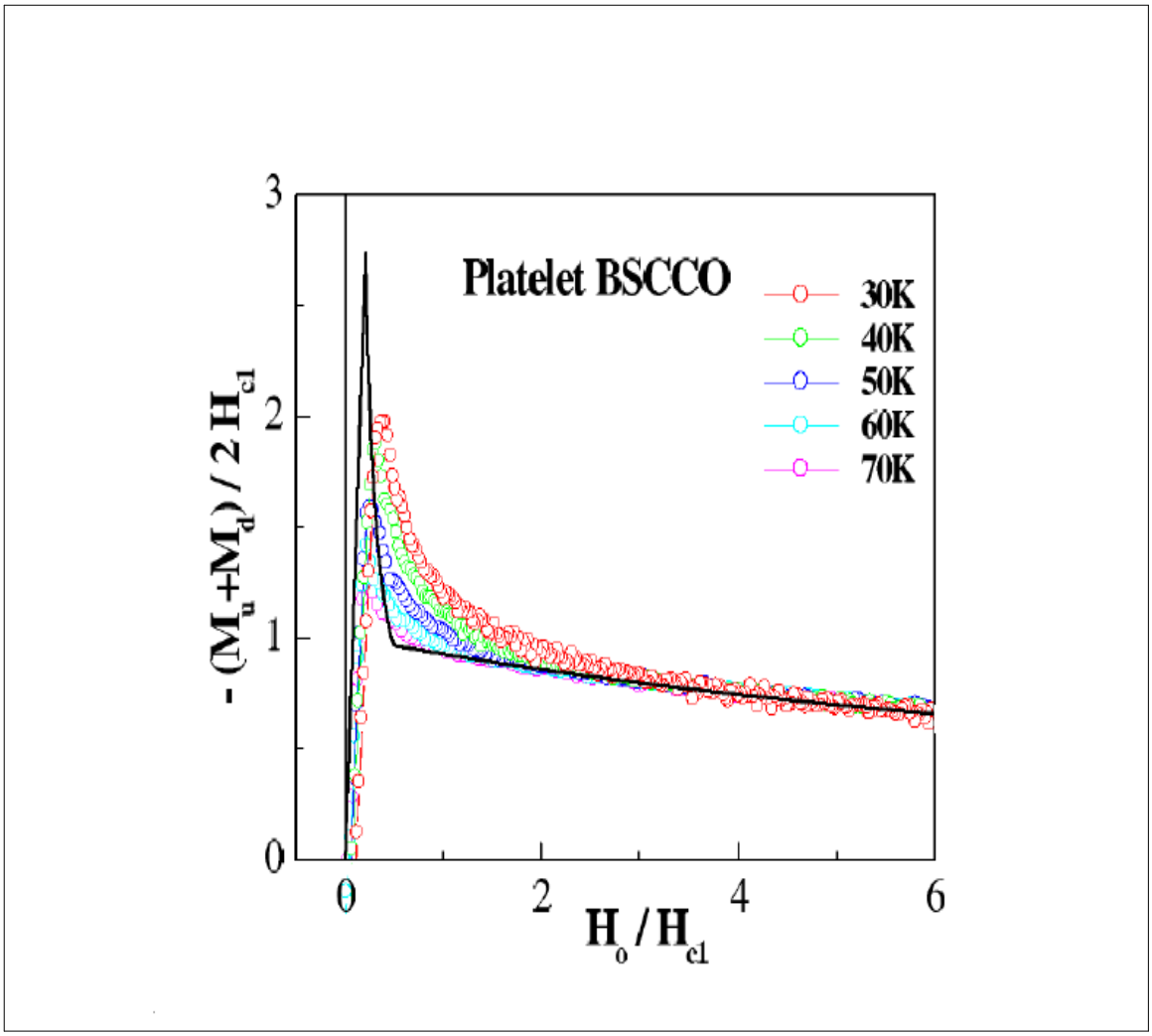


FIG. 4.10. Theoretical fit (solid curve) to experimental $(\overline{M} - H_0)$ , isotherms for the platelet specimen.

### 4.2.3 Procedure for the platelet YBCO Specimen

From the fundamental theory, where the parameter $\kappa$ is supposed to be independent of the temperature, $T$, we expect a single behavior. However, other possibilities exist as we will see in the following section. The fitting is done in two ways, namely:

1) We adjust $H_{c1}$ and $\kappa$ so that all curves are normalized onto a single common curve to get an average value for $\kappa$, as shown in Fig.4.11.

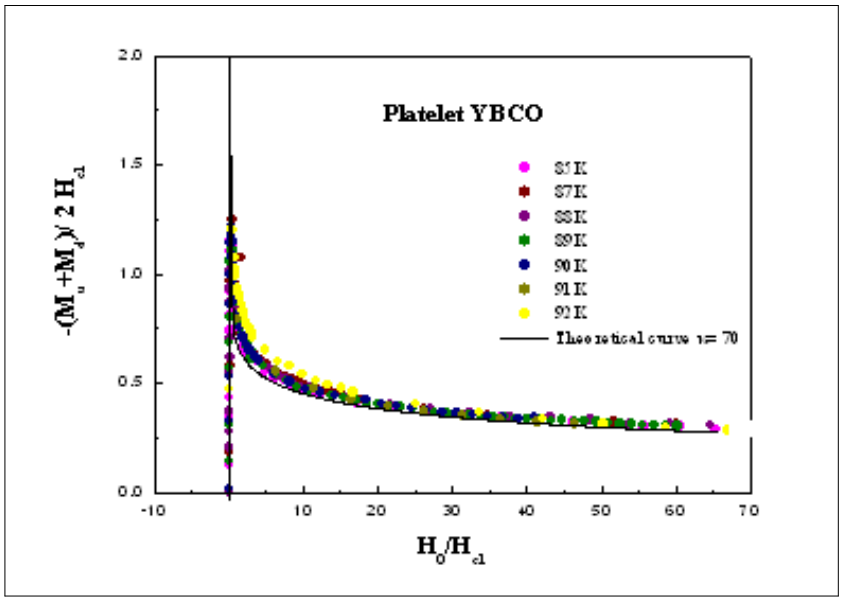


FIG. 4.11. Theoretical fit (solid curve) to experimental $(\overline{M} - H_0)$ isotherms for $\kappa = 70$ for the YBCO specimen.

2) We normalize each curve individually to the best fit, giving different values for $\kappa$, as shown in Fig. 4.12. We show each curve separately from Fig. 4.13- Fig. 4.19.

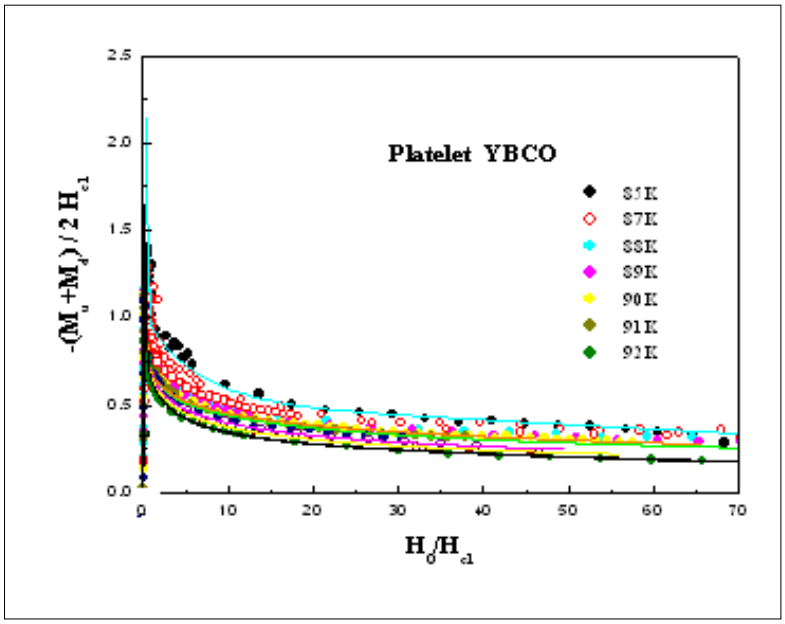


FIG. 4.12. Theoretical fits (solid curves) to experimental ($\overline{M} - H_0$) isotherms for the YBCO specimen.

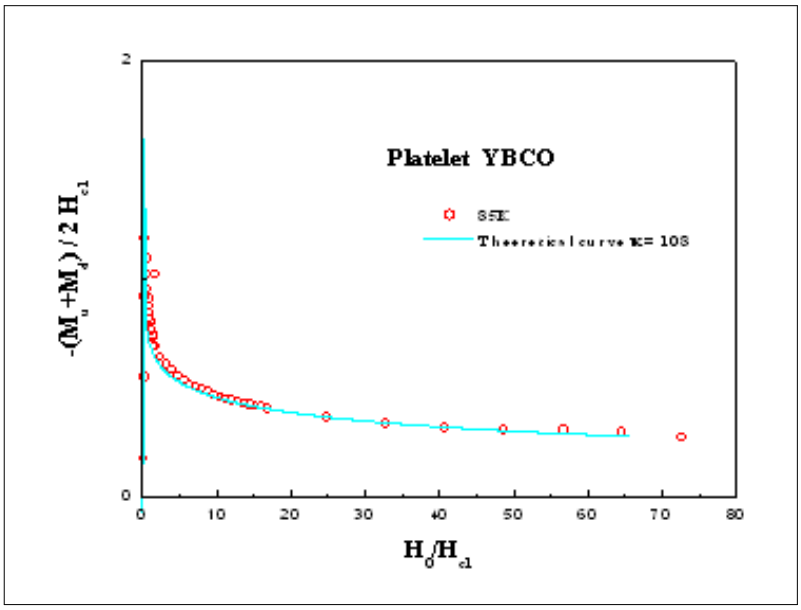


FIG. 4.13. Theoretical fit (solid curve) to experimental ($\overline{M} - H_0$), 85K isotherm for the YBCO specimen.

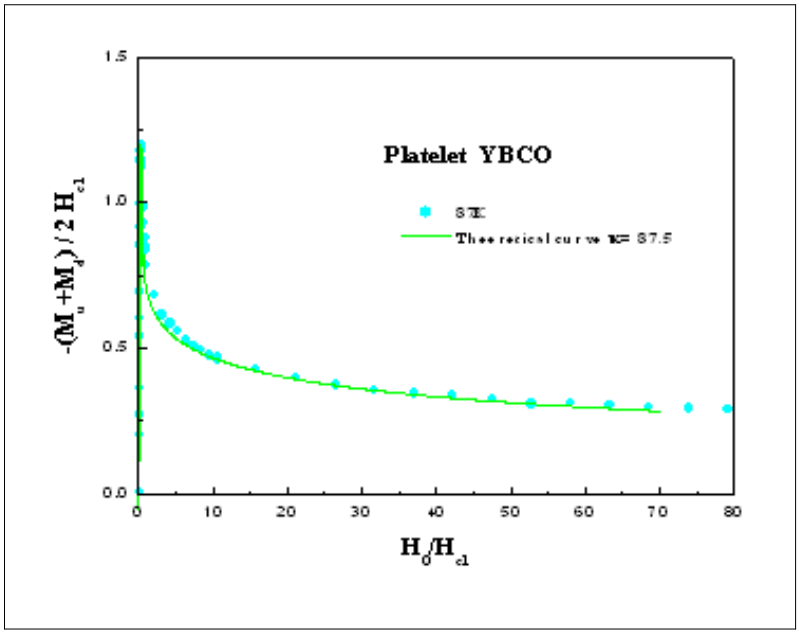


FIG. 4.14. Theoretical fit (solid curve) to experimental $(\overline{M} - H_0)$, 87K isotherm for the YBCO specimen.

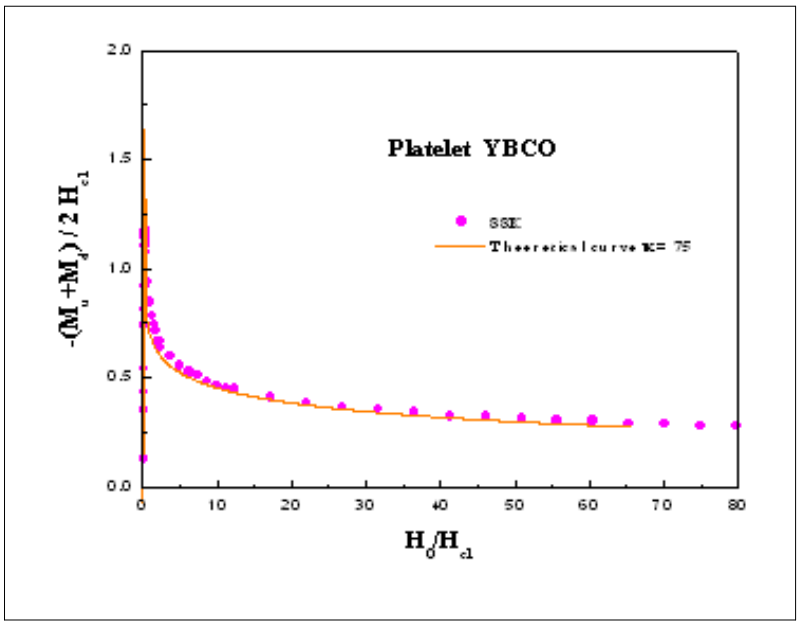


FIG. 4.15. Theoretical fit (solid curve) to experimental $(\overline{M} - H_0)$, 88K isotherm for the YBCO specimen.

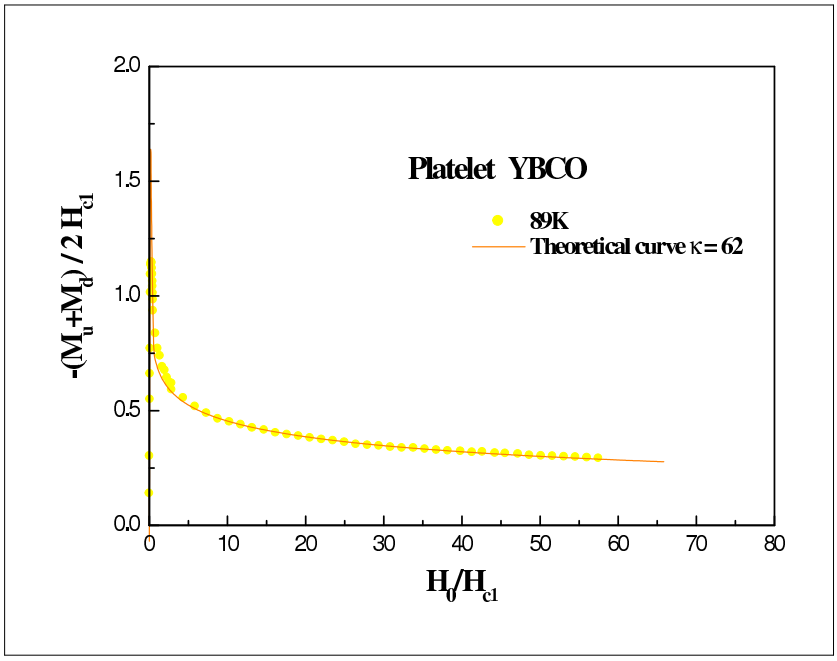


FIG. 4.16. Theoretical fit (solid curve) to experimental ($\overline{M} - H_0$), 89K isotherm for the YBCO specimen.

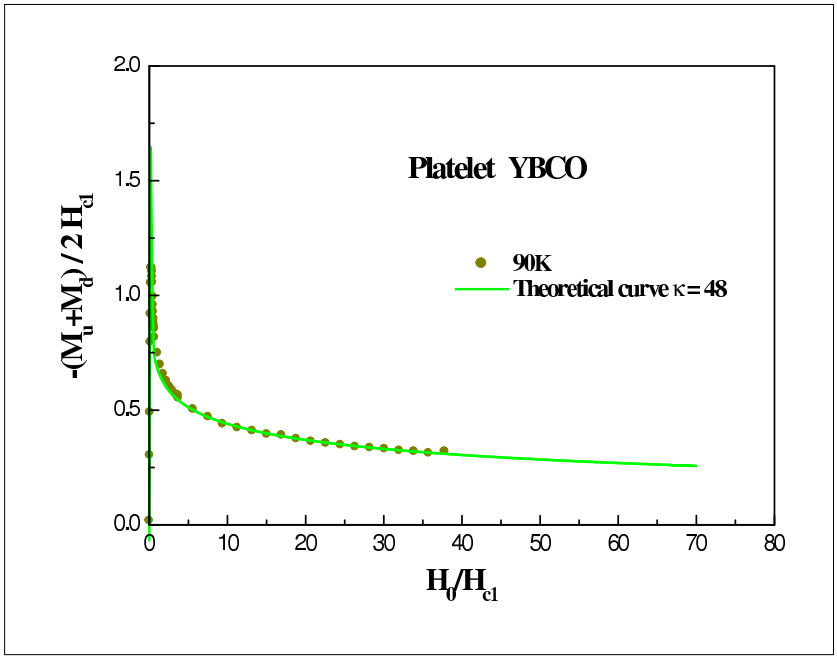


FIG. 4.17. Theoretical fit (solid curve) to experimental ($\overline{M} - H_0$), 90K isotherm for the YBCO specimen.

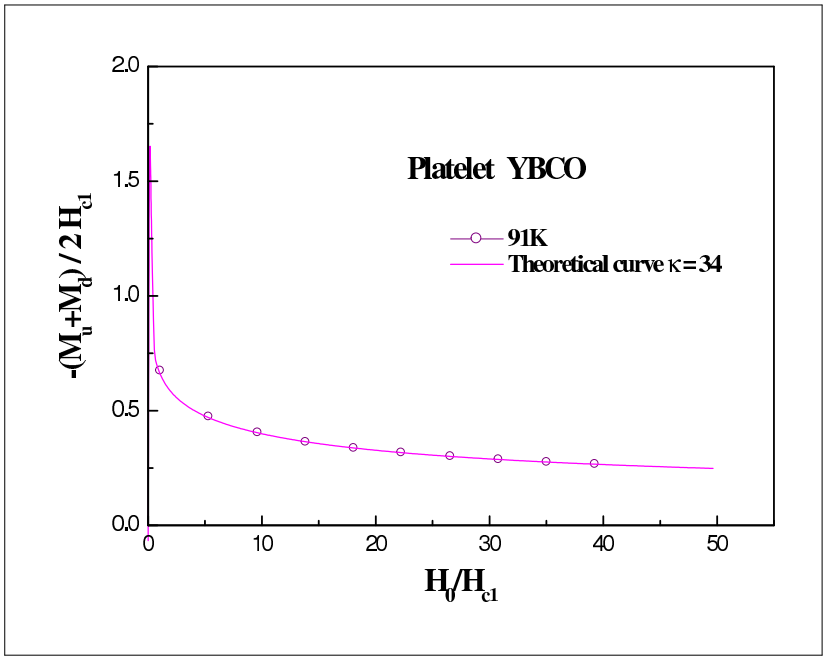


FIG. 4.18. Theoretical fit (solid curve) to experimental ($\overline{M} - H_0$), 91K isotherm for the YBCO specimen.

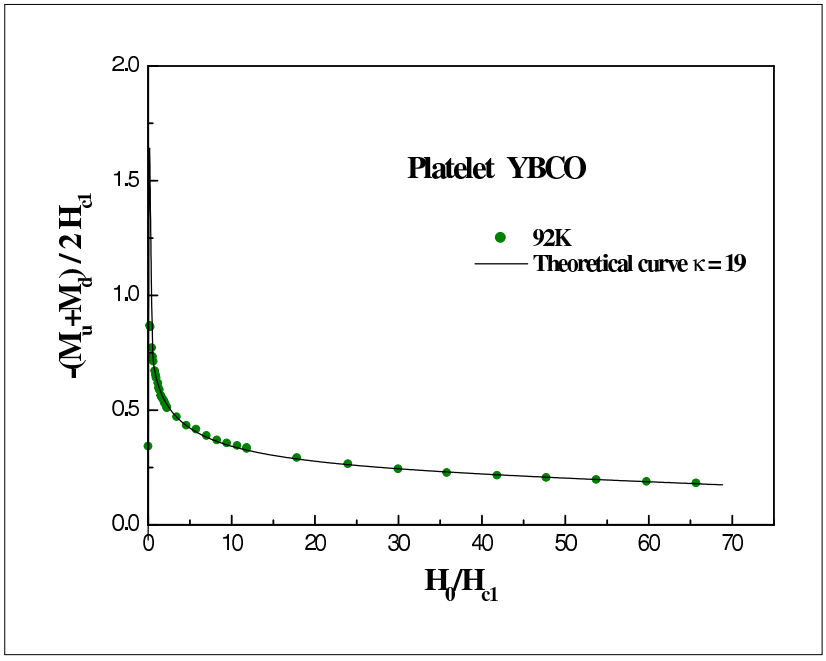


FIG. 4.19. Theoretical fit (solid curve) to experimental ($\overline{M} - H_0$), 92K isotherm for the YBCO specimen.

## 4.3 Temperature Dependence of Characteristics parameters

### 4.3.1 Lower critical field

As introduced previously, the method we use allows us to determine the values of the parameter $H_{c1}$ from the fits. The results obtained for the BSSCO (Disc and Platelet) and the YBCO specimens are presented in Tables 4.1 and 4.2 below.

TABLE. 4.1. Values of $H_{c1}$ for the BSCCO Specimens (disc and platelet).

| BSCCO | | |
|---|---|---|
| Disc | | Platelet |
| $T(K)$ | $H_{c1}(Oe)$ | $H_{c1}(Oe)$ |
| 30 | 212 | 198 |
| 40 | 198 | 185 |
| 50 | 175 | 166 |
| 60 | 150 | 142 |
| 70 | 115 | 110 |

TABLE. 4.2. Values of $H_{c1}$ for the YBCO Specimen for constant $\kappa$ and different $\kappa$.

| YBCO | | |
|---|---|---|
| Fixed $\kappa = 70$ | | Different $\kappa$ |
| $T(K)$ | $H_{c1}(Oe)$ | $H_{c1}(Oe)$ |
| 85 | 117 | 117 ($\kappa = 108$) |
| 87 | 93 | 93 ($\kappa = 87.5$) |
| 88 | 81 | 79 ($\kappa = 75$) |
| 89 | 68 | 62 ($\kappa = 62$) |
| 90 | 53 | 48 ($\kappa = 48$) |
| 91 | 38 | 31 ($\kappa = 34$) |
| 92 | 19 | 12 ($\kappa = 19$) |

The results for each specimen are respectively plotted in Fig.4.20 and Fig.4.21 below.

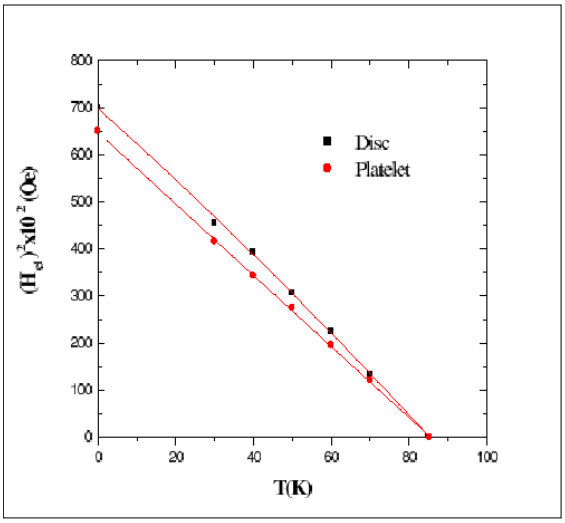


FIG. 4.20. The square of the lower critical field, $(H_{c1})^2$, as determined from the normalization of the magnetization isotherms for the BSCCO (disc and platelet) specimens.

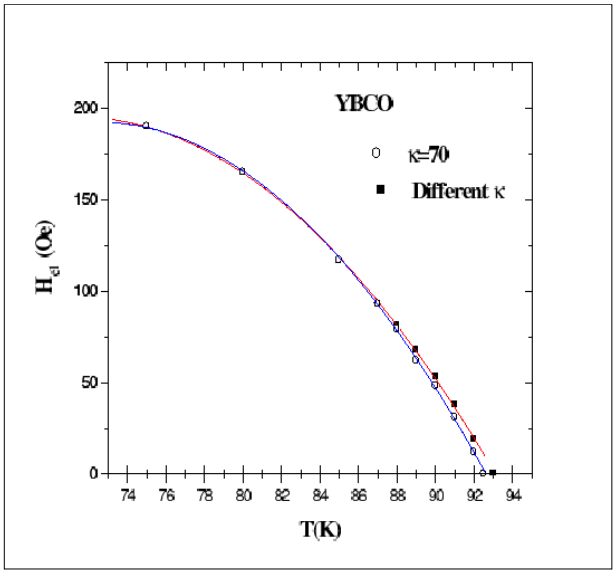


FIG. 4.21. The lower critical field, $H_{c1}$, as a function of $T$, as determined from the normalization of the magnetization isotherms for the YBCO specimen. The red curve shows the different values obtained for $H_{c1}$ with different values of $\kappa$, while the blue curve gives $H_{c1}$ obtained with a fixed value of $\kappa$ as explained in the previous section.

We notice that for the BSSCO specimen the results obtained for the disc are somewhat higher than for the platelet. These results can be fitted over the range of temperature investigated by the form: $H_{c1}(t) = H_{c1}(0)(1-t)^{1/2}$, $t = T/T_c$, with $H_{c1}(0) \cong 264$ Oe and $T_c \cong 85$K for the disc and $H_{c1}(0) \cong 255$ Oe and $T_c \cong 85.3$K for the platelet. This difference can probably be due to the possibility of a different oxygen stoichiometry in the disc and platelet BSSCO specimens. For the YBCO specimen the two curves are coincident at lower temperatures and become slightly different for temperature near the critical temperature $T_c$. It is then important to find out the reason behind the difference in $\kappa$ as $T \rightarrow T_c$. We think that this may be due to the size effect and will be considered later.

### 4.3.2 Ginsburg-Landau $\kappa$

In this section, we present the values of the Ginsburg-Landau parameter $\kappa$, as obtained from the normalization of the magnetization isotherms, in Fig. 4.22 below:

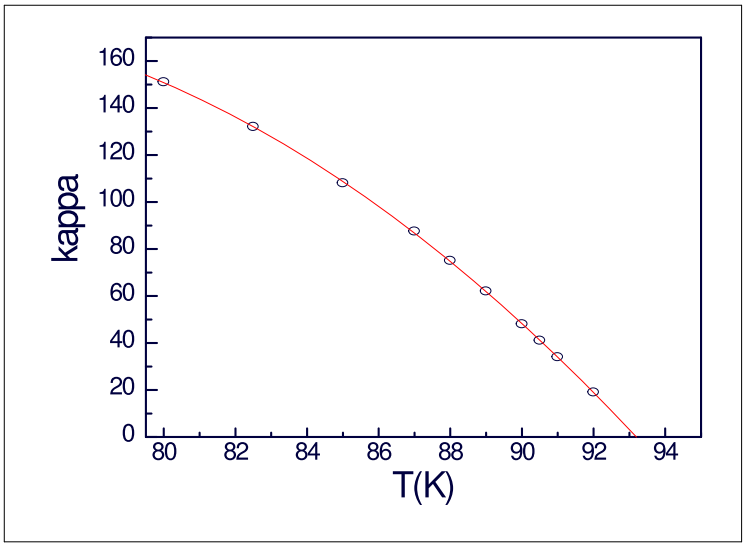


FIG. 4.22. The Ginsburg-Landau parameter, $\kappa$, as determined from the normalization of the magnetization isotherms for the YBCO specimen.

A feature of the G-L theory is that $\kappa$, is a non-zero constant near $T_c$. This is widely accepted. But this work finds a stray variation in $\kappa$, which seems to reach zero at $T_c$. This is a remarkable difference. This behavior should be of some theoretical interest and needs a further attention.

### 4.3.3 Discussion

In the previous section the fitted value of $\kappa$ decreases as $T \to T_c$ and possible reasons for this will now be discussed.

i) An obvious first possibility to consider is a size effect as the specimens are not very large in comparison with the penetration length $\lambda$ near $T_c$. In order to check it we are going to find the penetration length $\lambda(T \to T_c)$ and compare it with the size of the specimen, $\ell$. Various techniques, such as measurement of the susceptibility of powders of known size distribution [26], measurements of the spin resonance profile for trapped muons in the mixed state [35], and observations of frequency shift in microwave resonators [36], have been used to obtained the magnetic penetration depth in the cuprates. For our purpose, we use $\lambda_0 = 0.135\mu$m in order to represent the penetration depth $\lambda(T) = \lambda_0[1-(T/T_c)^4]^{-1/2}$. However, for the accuracy of our method, we must take in account the thickness of our specimen in order to see if it can be responsible of the unexpected decrease of $\kappa$, near $T_c$. We write $\dfrac{1}{\lambda_{eff}} = \dfrac{1}{\lambda} + \dfrac{1}{\ell}$ where $\lambda_{eff}$ is the effective penetration depth and $\ell$ the thickness of the specimen as illustrated in Fig. 4.23.

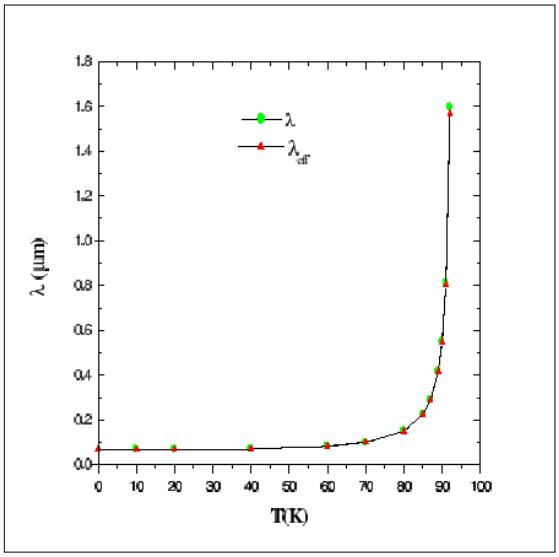


FIG. 4.23. The temperature dependence of the penetration depth $\lambda$ and the effective penetration depth $\lambda_{eff}$, for the YBCO specimen.

It is clear from Fig. 4.23 that there is not a big difference between the two curves. This can be explained by the fact that the thickness of our specimen, $\ell = 90.5\,\mu$m is bigger than $\lambda$. From the formula, if $\lambda \ll \ell \;\; \longmapsto \lambda_{eff} \simeq \lambda$. This means that within the dimensions of our specimen, we can use our method for the determination of the Ginsburg-Landau parameter $\kappa$.

ii) Another possibility can be the spatially inhomogeneous oxygen distribution resulting in spatially inhomogeneous $T_c$ and hence, near $T_c$ , spatial regions in the specimen gradually becoming normal with size effects in these regions becoming important and the model generally failing.

iii) Another possibility can be the changes in the vortex lattice structure (e.g., vortex lattice melting) near $T_c$.

# Chapter 5

# CONCLUSIONS

The problem of the determination of the equilibrium behavior in the high-$T_c$ superconducting systems has been briefly reviewed and the analysis of the magnetization behavior has been described in some detail. The theory was applied to experimental $M$ versus $H_0$ isotherms for the YBCO and BSCCO single crystals with platelet and disc geometry, with the applied field, $H_0$ directed along the c-axis in these thin crystals. The constitutive $B^{rev}(H,T)$ relations, the lower critical field, $H_{c1}(T)$ and the Ginsburg-Landau parameter $\kappa$, were determined.

In the G-L analysis, which is strictly valid only near $T_c$, $\kappa$ is independent of temperature. In the present study of an YBCO specimen in temperature regime near $T_c$ it was found that better fits of experimental $M-H$ data to the present Ginsburg-Landau treatment were obtained when $\kappa$ was treated as a free fitting parameter for each temperature rather than a fixed fitting parameter for all temperatures, which in the present study was $\kappa = 70$. This is shown in Fig. 4.11 and Fig. 4.12 respectively. In the temperature regime of the present experimental data, (i.e. $80\,\mathrm{K} < \mathrm{T} < 93\,\mathrm{K}$) $\kappa$ was found to decrease from about 150 at 80K to about 18 at 92K (Fig. 4.22). This behavior, in consideration of the G-L theory seems to be, on first consideration anomalous, and, if valid, requires explanation. In this respect possible reasons for the apparent decrease in $\kappa$ near $T_c$ were given.

We investigated the possibility of a size effect which would be manifest in the regime near $T_c$ where $\lambda$ is increasing rapidly with temperature and become of the same order of magnitude as the appropriate specimen dimension and we found that the effect is inadequate. A second possibility to explain this could be the spatially inhomogeneous oxygen distribution. The third possibility requires a detailed investigation, which is beyond the scope of the present thesis. It does have the merit that it is well known [2, 37, 38, 39] that, under certain conditions, there is a vortex lattice melting transition in YBCO in the $H-T$ plane presently investigated. The effects of this transition on $\kappa$ have not been previously published but the vortex lattice transition in BSSCO certainly does lead to a large decrease in $\kappa$. In the present study on the BSCCO disc specimen three different regions of the $(B, T)$ plane, with different, but constant values for $\kappa$, corresponding to the arrowhead regime ($\kappa = 250$), the solid vortex phase ($\kappa = 70$) and the liquid vortex phase ($\kappa = 3$) were identified. The behavior of $\kappa$(T) in the YBCO specimen near $T_c$ may then, in terms of the behavior in the BSSCO disc specimen be due to a gradual vortex lattice melting transition in the $H - T$ plane, near $T_c$ of the present investigation.

The platelet BSSCO specimen, of different oxygen stoichiometry showed no distinct solid/liquid vortex lattice transition and was fitted over the entire $(B - T)$ plane (in the superconducting regime) with $\kappa = 70$. [It is, however, possible but was not presently investigated, that fits to the experimental $M - H$ data for the platelet specimen might have been improved with different values for $\kappa$ over the entire $(B\,, T)$ plane. Such differences would, however, in view of the very close fits obtained with a constant value for $\kappa$, be relatively small.]

As we saw in the previous chapters, it is not easy to measure the critical fields of cuprate superconducting systems directly. Magnetization measurements provide the only reliable values, but relatively few have been made. Direct measurements of $H_{c1}$ are equally difficult because of the problem of removing the surface barrier to flux entry in cuprate materials, and tend to be too high. Many published solutions to the problem rely on indirect methods and approximations. Hence, the present work provides a novel technique (to the best of our knowledge) that demonstrates that the determination of $H_{c1}(T)$ from magnetization measurements is more reliable than the usual method of estimating the point of deviation from the Meissner behavior because it is derived self-consistently from bulk equilibrium $m^e(h_0)$ behavior and is not influenced by bulk or surface vortex pinning, specimen shape, surface-

barrier or anisotropy effects. This analysis yields accurate values for the lower critical field $H_{c1}(T)$ and the Ginsburg-Landau parameter $\kappa$. The determination of characteristics parameters $H_{c1}$, $H_{c2}$, $\kappa$, through techniques such as the one in the present investigation, would be an important step towards the commercial application of superconductors like YBCO, BSCCO, $MgB_2$ etc ...

# Bibliography


[1] H. K. Onnes, Commun. Phys. **24C** (1911).

[2] C. Kittel, *Introduction to Solid State Physics* (John Wiley and Sons. Ltd, 1986).

[3] V. L. Ginzburg and L. D. Landau, ZH. Eksp. Teir. Fiz **20**, 1064 (1950).

[4] A. A. Abrikosov, Zh. Eksp. Teor. Fiz **32**, 1442 (1957).

[5] J. Bardeen, L. N. Cooper, and J. R. Schrieffer, Phys.Rev **106, 108**, 162, 1175 (1957).

[6] O. Madelung, *Introduction to solid state theory* (Springer-Verlag, Berlin, 1978).

[7] B. D. Josephson, Rev. Mod. Phys **46** (1974).

[8] J. G. Bednorz and K. H. Müller, Z. Phys. B **64**, 189 (1986).

[9] C. W. Chu *et al.*, Nature **365**, 323 (1993).

[10] D. R. Harshman and A. P. Millis, Phys. Rev. B **45**, 10684 (1992).

[11] M. Tinkam, J. Shira, and E. Castellano, *Introduction to Superconductivity* (McGraw-Hill Publishing Company, 1996).

[12] C. J. Gorter and H. B. G. Casimir, Z. Phys. **35**, 963 (1934).

[13] F. London and H. London, Proc. R. Soc. A **149**, 71 (1935).

[14] M. Cyrot and D. Pavuna, *Introduction to Superconductivity and High-Tc Materials* (World Scientific Publishing, 1992).

[15] R. Labusch and T. B. Doyle, 6th european conference of applied superconductivity, 181, Inst. Phys., Sorrento, Italy, 2003.

[16] Z. Hao *et al.*, Phys. Rev. B **43**, 2844 (1991).

[17] T. B. Doyle, PhD thesis, University of the Witwatersrand, 1975 (Unpublished).

[18] R. Labusch and T. B. Doyle, Physica C **290**, 143 (1997).

[19] T. B. Doyle, R. Labusch, and R. A. Doyle, Physica C **290**, 148 (1997).

[20] C. P. Bean and J. D. Livingstone, Rev. Mod. Phys. **36**, 31 (1964).

[21] K. E. Gray, R. T. Kampwirth, and D. E. Farrell, Phys. Rev. B **41**, 819 (1990).

[22] R. A. Doyle *et al.*, Physica C **308**, 123, 131 (1998).

[23] C. D. Dewhurst *et al.*, Phys. Rev. B **53** (1996).

[24] Foner, Review of Scientific Instruments **30**, 548, 557 (July 1959).

[25] J. R. Waldram, *Superconductivity of metals and cuprates* (Institute of Physics, 1996).

[26] G. Burns, *High Tc Superconductivity, An Introduction* (Academic Press, 1992).

[27] M. McElfresh, *Fundamentals of magnetism and magnetic measurements featuring Quantum Design's magnetic property measurement system* (Quantum Design, 1994).

[28] K. Kadowaki, T. Mochiku, H. Takeya, Y. Saito, and K. Hirata, J.Supercond. **8**, 461 (1995).

[29] G. Balakrishnan, D. M. Paul, M. R. Lees, and A. T. Boothroyd, Physica C **206**, 148 (1993).

[30] R. L. Peterson and J. W. Ekin, Phys. Rev. B **37**, 9848 (1988).

[31] X. jun Yu and M. Sayer, Phys. Rev. B **44**, 2348 (1991).

[32] B. Khaykovich *et al.*, Phys. Rev. Lett. **76**, 2555 (1996).

[33] H. Pastoriza, M. f. Goffman, A. Arribere, and F. D. la Cruz, Phys. Rev. Lett. **72**, 2951 (1994).

[34] E. Zeldov *et al.*, Nature **375**, 373 (1995).

[35] B. R. Coles, *Advances in Physics* (Taylor and Francis Limited, 1972).

[36] Y. Simon and P. Thorel, Phys. Lett. A **35**, 450 (1971).

[37] H. Safar *et al.*, Phys. Lett **69**, 824, 828 (1992).

[38] W. K. Kwok *et al.*, Phys. Lett **69**, 3370 (1992).

[39] W. K. Kwok *et al.*, Phys. Lett **72**, 1092, 1096 (1994).

[40] C. P. Poole, H. A. Farach, and J. R. Creswick, *Superconductivity* (Academic Press Ltd, 1995).

[41] E. Zeldov *et al.*, Phys. Rev. Lett **73**, 1428 (1994).

[42] C. P. Bean, Phys. Rev. Lett **8**, 250 (1962).

[43] E. H. Brandt, Phys. Rev. Lett **78**, 2208 (1997).

[44] B. Seeber, *Handbook of Applied Superconductivity* (Institute of Physics Publishing Bristol and Philadelphia, 1998).

[45] G. Blatter, M. V. Feigelman, V. B. Geshkenbein, A. I. Larkin, and V. M. Vinokur, Rev. Mod. Phys **66**, 1125 (1995).

[46] T. B. Doyle, PhD thesis, University of the Witwatersrand, 1975.

[47] J. Frankel, J. Appl. Phys **50**, 5402 (1979).

[48] M. V. Indenbom *et al.*, 7th international workshop on critical currents in superconductors, p. 117, World Scientific, Albach, Austria, 1994.

[49] M. Benkraouda and J. R. Clem, Phys. Rev. B **53**, 5716 (1996).

[50] T. Schuster, M. V. Indenbom, H. Kuhn, E. H. Brandt, and Konczykowski, Phys. Rev. Lett **73**, 1424 (1994).

[51] R. A. Klemm and J. R. Clem, Phys. Rev. B **21**, 1868 (1980).

[52] T. V. Duzer and C. W. Turner, *Principles of Superconductive Devices and Circuits* (Elsevier North Holland, 1981).

[53] A. M. Campbell and J. E. Evetts, *Critical currents in superconductors* (Taylor Francis Ltd, 1972).

[54] V. G. Kogan, Phys. Rev. B **24**, 1572 (1981).

[55] U. Welp *et al.*, Phys. Rev. Lett. **62**, 1908 (1989).

[56] D. X. Chen, J. A. Brug, and R. B. Goldfard, IEEE Trans. Magn. **27**, 3601 (1991).

[57] T. Mochiku and K. Kadowaki, Trans. Mater. Res. Soc. **19A**, 349 (1993).

[58] J. Evetts, *Concise Encyclopedia of Magnetic and Superconducting Materials* (Oxford, 1992).

[59] R. G. Goldfard, M. Lelental, and C. A. Thompson, *Magnetic Susceptibility of Superconductors and Other Spin Systems* (Plenum Press, New York, 1992).

[60] J. A. Osborn, Phys. Rev. **37**, 3751 (1945).

[61] F. J. Blunt, A. R. Perry, A. M. Campbell, and R. S. Liv, Physica C **175**, 539, 544 (1991).

[62] M. McElfresh, L. Shi, and R. Sager, *Effects of magnetic field uniformity on the measurement of Superconducting Samples* (Quantum Design, 1996).

[63] J. Matricon and D. Saint-James, Phys. Lett. A **24**, 241, 242 (1967).

[64] J. W. Ekin, H. R. Hart, Jr, and A. Gaddipati, J. Appl. Phys. **68**, 2285.

[65] H. Dersch and G. Blatter, Phys. Rev. B **38**, 391 (1988).

[66] J. Provost, E. Paumier, and A. Fortini, J. Phys. **4**, 439 (1974).

[67] C. P. Bean and J. D. Livingston, Phys. Rev. Lett. **12**, 14 (1973).

[68] P. W. Anderson and Y. B. Kim, Rev. Mod. Phys. **36**, 39, 43 (1964).

[69] P. H. Kes, *Phenomenology and Applications of High Temperature Superconductors* (Addison-Wesley, New York, 1992).

[70] T. B. Doyle *et al.*, Physica C **332**, 365, 369 (2000).

[71] A. B. Pippard, Proc. Roy. Soc **A216**, 547 (1953).